Investigating High-Efficiency Thermoelectric Materials:

Chalcogenide GeTe and Skutterudite $Co_4Ge_6Te_6$

Investigating High-Efficiency Thermoelectric Materials:

Chalcogenide GeTe and Skutterudite $Co_4Ge_6Te_6$

by

Leon Yuyang Huang, B.Sc. (Honours)

A thesis submitted to the School of Graduate Studies

In partial fulfillment of the requirements for the degree

MASTER OF SCIENCE

McMaster University

Hamilton, Ontario

2022

MASTER OF SCIENCE (2022)

Department of Chemistry and Chemical Biology

TITLE: Investigating High-Efficiency Thermoelectric Materials: Chalcogenide GeTe and Skutterudite $Co_4Ge_6Te_6$

AUTHOR: Leon Yuyang Huang, B. Sc. (Honors) (McMaster University)

SUPERVISOR: Professor Yurij Mozharivskyj

NUMBER OF PAGES: xi, 87

Abstract

The focus of this research is to explore high-efficiency thermoelectric materials, which can be put into daily application to mitigate the energy crisis. Some fundamentals and modern characterization techniques are briefly discussed.

Due to their ability to convert waste heat into electricity, thermoelectric materials have drawn significant attention in the past two decades. The most widely used thermoelectric materials nowadays are still composed of Pb and Te. Due to the toxic nature of Pb, extensive work has been done on the GeTe system, an environmentally friendly replacement for PbTe. Unfortunately, the pristine GeTe suffers from a high carrier concentration originating from the low formation energy of Ge vacancies. Herein, the introduction of ZnO nanoparticles into the GeTe matrix to form ZnTe nanophase resulted in the suppression of carrier concentration. This simultaneously increased the average Seebeck coefficient by 40% and achieved a substantial reduction (33%) in electrical thermal conductivity below 600K when compared to a pure GeTe. As a result, the peak zT reached 1.44 at 690K in the 1.5*wt.%* ZnO sample, and an average *zT* value was increased by 23% to 0.79 in the 323-733K range.

By adopting partial substitution of Fe at the Co site in the $Co_4Ge_6Te_6$ ternary skutterudites, $Co_{4-x}Fe_xGe_6Te_6$ (x=0.04 and 0.12) was successfully tuned from an *n*-type

material into a *p*-type one as proven by the positive Seebeck coefficient. An enhanced electrical conductivity was achieved by increasing the carrier concentration.

Acknowledgments

Time passed quickly; it had been three years since I started as a summer volunteer in Dr. Yurij's research lab. Until I write this page, my journey to research high-efficiency thermoelectric materials is about to end. Research is fun, and we celebrate every achievement as we push the boundary of knowledge. Research is hard, and I appreciate every warm help and support from each individual who has helped me along the road.

I sincerely thank my supervisor, Dr. Yurij Mozharivskyj, for his support at all times. Your knowledge and insight lay the foundation for the success of my projects. Thank you for patiently forgiving my mistakes and providing an excellent environment for researching and learning. I also want to express my gratitude to Dr. Yu-Chih Tseng. Thank you for the continuous help by measuring countless (42) samples during the most challenging time. And I want to thank my committee member Dr. John Greedan for his wise advice.

I want to thank my amazing colleagues. It has been a rewarding experience for me to work with all of you. Working with my research partner, a Ph.D. candidate, Zan Yang, I learned a lot. I thank Ph.D. candidate Shaochang Song for being my mentor during my undergraduate thesis. I thank Ph.D. candidates Timothy Lo and Sergei Novikov for sharing their knowledge.

I want to especially thank my wife Olivia and my little one DouDou for you being the pillar of my life and for my mental sustainability. You are my joy. I want to thank my parents for their always support.

Table of Content

List of Figures and Tables

Chapter 1. Introduction of Thermoelectric

Owing to the global energy crisis, finding sustainable and green energy sources is the united goal of the entire human race. Thermoelectric (TE) technology is an ideal path for power generation and cooling as it enables solid-state interconversion of heat and electricity by employing the Seebeck and Peltier effects.[1,2] TE technology offers robustness with the advantages of high power density, extensive scalability, and motionless operation.

1.1 Discovery of Thermoelectric Materials

Thermoelectric materials are governed by three phenomena, Seebeck, Peltier, and Thomson effects. In 1821, Thomas Johann Seebeck observed a magnetic field when he applied a thermal gradient to a junction of two dissimilar metals, as evidenced by a flip of a compass needle.[3] And the degree of the needle deflection was found to be proportional to the temperature gradient between the metal junctions. As a result, he characterized this effect as thermomagnetism. However, it was not until 1834 that Danish scientist Hans Christian Orsted correctly explained Seebeck's observations of thermoelectricity; the magnetic field was generated by the current, which in turn was produced by the thermal gradient.[4]

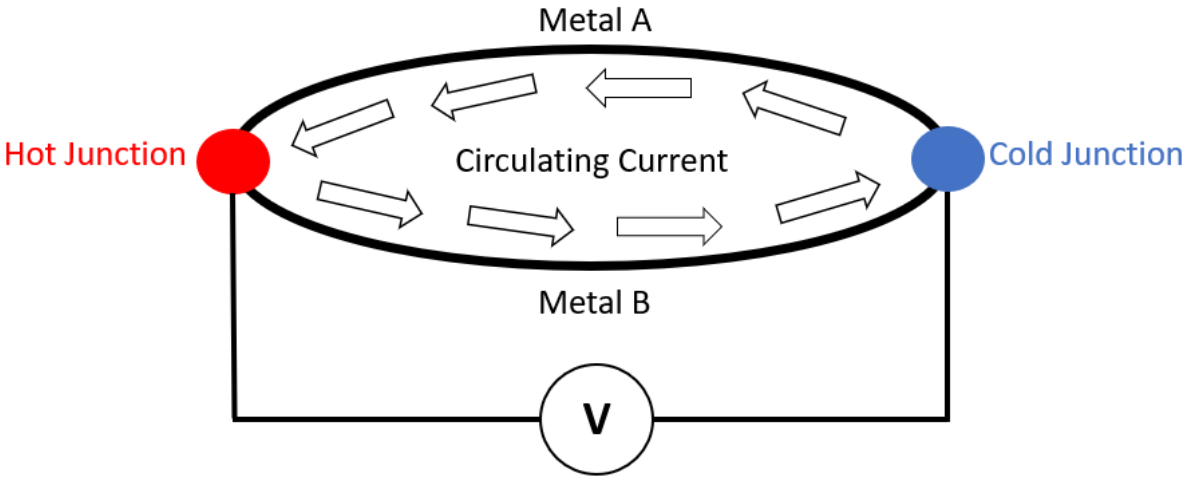

Figure 1.1 Scheme diagram of Seebeck effect producing current on two unlike metals with an applied temperature gradient.

The Seebeck coefficient (S, α) or thermopower describes the change in the voltage (ΔV) over the temperature gradient (ΔT) in a given distance.[5]

$$\alpha = -\frac{\Delta V}{\Delta T} \qquad (1\text{-}1)$$

The thermal energy at the hot junction makes the electric carriers diffuse from the hot end to the cold end. This thermal diffusion will continue until the thermal flow of the carriers is offset by the electrostatic discharge.[6] Since two different materials have distinct carrier mobility, a chemical potential (voltage) will be generated; this effect is widely utilized in bimetallic thermocouples.

The Drude theory, based on the kinetic theory of gasses, was originally applied to explain the thermoelectric effect. However, it overestimated the Seebeck effect by a factor

of 100 for the metals and could not explain the origin of the positive Seebeck effect. The values of the thermopower can be adequately estimated if the Fermi-Dirac distribution is employed. According to the Fermi-Dirac distribution, only fermions within a specific energy range $\frac{k_B T}{E_F}$ will attribute to the properties of a material, where k_B, T, E_F is Boltzmann constant, temperature and Fermi level energy respectively[7,8]. Next, one has to employ the nearly-free electron model to explain the origin of the positive Seebeck coefficient. Bands built from the Bloch wavefunctions[9] have different curvatures; the valence band curves down, and the conduction band curves up in the *E* vs. *k* space (*k* is a wave vector in the reciprocal space). Since the mass of the charge carriers is proportional to the second derivative of the energy with respect to the k-vector[10]

$$m = \hbar^2 \left(\frac{d^2 E}{dk^2}\right)^{-1}, \tag{1-2}$$

electrons at the conduction band maximum (CBM) will have a negative effective mass and behave differently from electrons in the crystal lattice. To avoid the concept of negative mass, the electron with negative mass is assumed to be a particle with a positive mass and positive charge. This particle is called a hole. The existence of holes can explain the positive value of Seebeck in materials and semiconductors. As a result, semiconductors are

termed n-type and p-type as their dominant charge carriers are electrons or holes, respectively.

In 1834, French scientist Jean Charles Athanase Peltier discovered the second thermoelectric phenomenon.[11] He applied electrical current to a loop made of two dissimilar materials and observed a formation of a temperature gradient between the two junctions. This process was the reverse of the Seebeck effect. Russian scientist Heinrich Friedrich Emil Lenz further advanced Peltier's work in 1839 when he discovered the connection between heat transfer and the current direction in a circuit.[12] The Peltier effect can be mathematically expressed through the Peltier coefficient Π, the amount of heat, Q, evolved at a junction, and current, I, applied.[13]

$$\Pi = \frac{Q}{I} \tag{1-3}$$

Peltier coefficient is related to the Seebeck coefficient via temperature as given below,

$$\Pi = \alpha T. \tag{1-4}$$

The Thomson effect, the last thermoelectric phenomenon, was discovered by British physicist William Thomson.[14] It states a process of heat change would occur in a single type of semiconductor with a temperature gradient and a current passing through it simultaneously.[14] Thomson effect specified the relationship among the amount of heat

being produced, Q, for a given length of a non-isothermal segment, l, with a current density of J.

$$\frac{\partial Q}{\partial T} = -KJ\nabla T = -KJ\frac{\partial T}{\partial l} \tag{1-5}$$

K is the Tomson factor, which can be related to Seebeck and Peltier to form the following relationships,

$$K = T\frac{d\alpha}{dT} = \frac{d\Pi}{dT} - a \tag{1-6}$$

Significant advances in the thermoelectric field were not made until 1957. That year, Abram Fedorovich Ioffe concluded that an excellent thermoelectric material should have a considerable Seebeck coefficient, a, to maintain a voltage difference, good electrical conductivity,σ, for a charge carrier transport, and ultra-low thermal conductivity, κ, to hold the temperature gradient at the same time. These factors were then combined into a unit-less state-of-art figure of merit zT, the efficiency parameter of a thermoelectric material with a given temperature T,[15]

$$zT = \frac{\alpha^2\sigma}{\kappa}T. \tag{1-7}$$

This was the time when the foundations for thermoelectric research were established, and the focus in the field shifted from metal conductors to semiconductors and semimetals for

their extraordinary power factor $\alpha^2\sigma$, and this direction is still dominant in today's research.[16]

1.2 Applications of Thermoelectric Materials

The early thermoelectric applications came out in the 1950s and 1960s, and the old TE modules were mainly composed of Bi_2Te_3, BiSb, and PbTe.[17-19] Even though they pronounced their significance in commercial and military fields[17-19], they suffered from low efficiency, as their figure of merit hardly exceeded 1, equivalent to an 11% efficiency under working temperatures of 300K-600K. As a result, thermoelectric applications shine best in the fields where robust operation and compactness outweigh power generation efficiency compared to other energy sources.

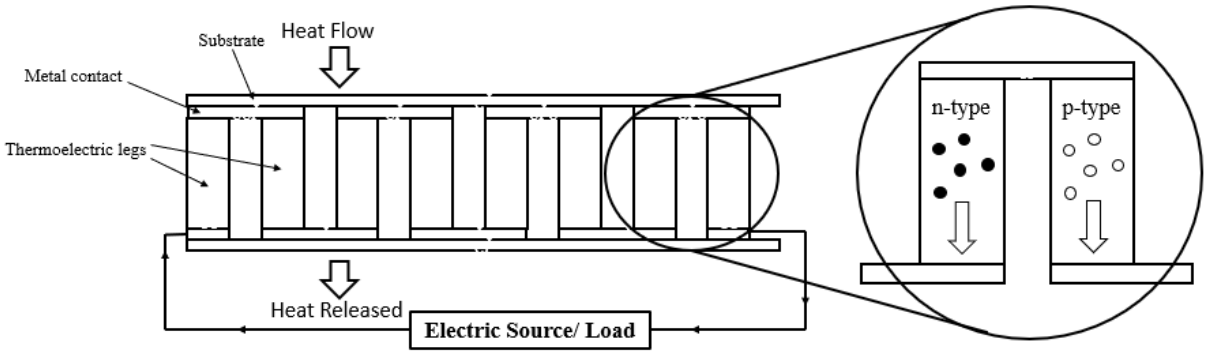

Figure 1.2 Model of a basic thermoelectric device constructed with n-type and p-type thermoelectric legs in the circuit.

A thermoelectric module is constructed from both *n*-type and *p*-type materials, which are connected electrically in series and thermally in parallel, as shown in Figure 1.2. When a temperature gradient is present, both electrons and holes can migrate from the hot end to the cold end, thus generating the current. Or, when the device is connected to a circuit, one side will cool down, and the other will heat up. However, finding high-performance *p*-type and *n*-type materials is difficult, as both materials must reach their optimal ZT values at the same working temperature. Moreover, the current can vary peak efficiencies among different temperatures and materials. Herein, the concept of compatibility factors for power generation[20, 21] suggests an excellent thermoelectric device should have the compatibility factor, s, within two or less.

$$s = \frac{(\sqrt{1 + zT} - 1)}{\alpha T} \tag{1-8}$$

The increasing demand for green energy has raised research interest in thermoelectric materials, and some significant advantages have been made over the last two decades. Even though thermoelectric materials still suffer from low efficiency, they possess other suitable properties such as portability, quietness, long-time operation, and relatively low operational cost. Small-scale electronic devices such as CCD cameras and

laser diodes utilize thermoelectric constructions for cooling and many other specialized products, including wristwatches[22], wood stoves[23], lamps[23,] and cooking pots[24].

One outstanding aspect of thermoelectric devices is their ability to operate over an extended time without any maintenance due to the lack of moving parts, which is essential for underground, submarine, and deep space exploration[25]. One great example is radioisotope thermoelectric generators (RTGs) used on spacecrafts and rovers; Mars rover Curiosity, Cassini, and Voyager 1 and 2 spacecrafts.[26]. In the RTGs, the heat released from the radioactive decay of Pu^{238} and outer space provide a temperature gradient and power for the space mission. Since the half-life of Pu^{238} is 87.7 years, which translates into less than 1% of electricity loss every year, RTGs can supply power for many years and even decades.

One of the most attractive applications of thermoelectric materials is the conversion of waste heat into usable energy. Many small and large-scale processes produce significant amounts of heat that are directly expelled into the environment; e.g., the energy losses in vehicles with internal combustion engines are around 60%[25]. Not surprisingly, the ability to convert waste heat into electricity by thermoelectric materials has attractive significant attention.

1.3 Thermoelectric Efficiency

Power generating efficiency, η, of thermoelectric materials is given by the following formula:

$$\eta = \frac{T_H - T_C}{T_H} \frac{\sqrt{1+ZT}-1}{\sqrt{1+ZT}+\frac{T_C}{T_H}} \quad (1\text{-}9)$$

where T_H and T_C are temperatures of the hot and cold ends. To make the efficiency η equal to the Carnot efficiency $\frac{T_H - T_C}{T_H}$, the ZT value would need to be infinite, which is apparently not possible. To make thermoelectric material as appealing as other sources of electricity production, an average ZT of 4 ought to be achieved.[27]

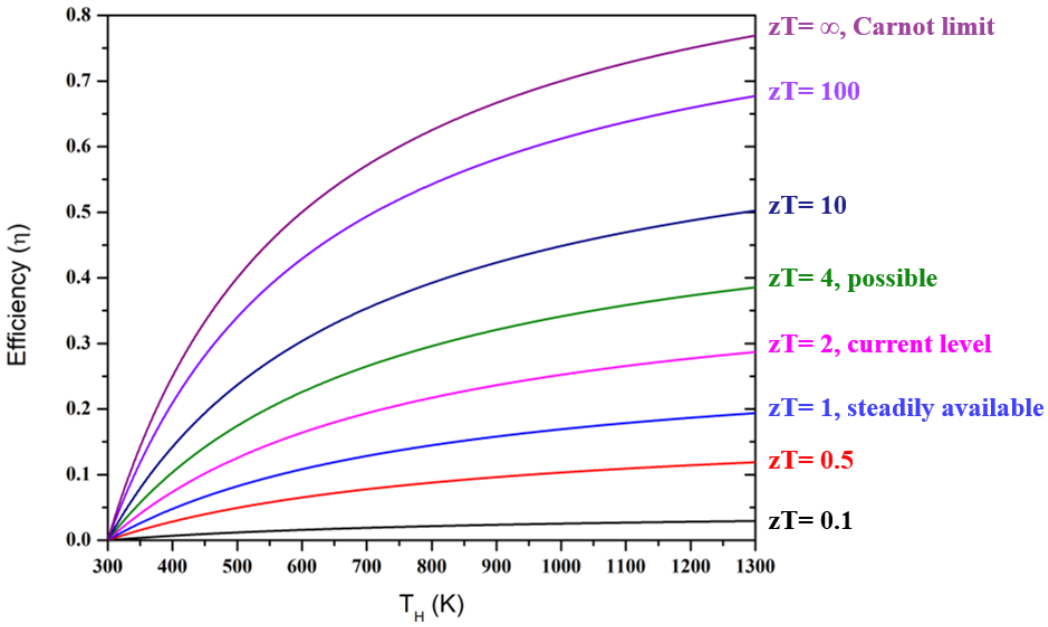

Figure 1.3. Thermoelectric efficiency to the temperature gradient and the figure of merit zT (T_c= 300K, room temperature)

1.3.1 Optimization of the Power Factor

A high Seebeck coefficient and electrical conductivity are essential to reach maximum efficiency. Good electrical conductivity will minimize the materials' intrinsic Joule heating, which is inevitable when a current passes through a conductor and thus creates unfavorable heat to diminish the temperature gradient.[28] The electrical conductivity of a material is directly related to the carrier concentration n, the charge of the carrier, and carrier mobility μ.

$$\sigma = ne\mu \tag{1-10}$$

Metals are the most conductive solids due to high carrier concentration and significant carrier mobility. Since metals don't have a band gap at the Fermi level, they are conductive even at extremely low temperatures. They experience a reduced electrical conductivity with the increasing temperature when atomic vibration starts to interfere with carrier propagation.[29] On the other hand, semiconductors and insulators have a finite band gap prohibiting electrical conduction at low temperatures. Charge carriers can overcome the band gap when the temperature rises and populate the conduction band. One can observe an exponential increase in electrical conductivity for semiconductors with temperature. Intrinsic semiconductors are the ones with high purity and will typically follow the conductivity curve mentioned before. In contrast, extrinsic semiconductors are often

heavily doped with impurities and display relatively good electrical conductivity even at low temperatures, which declines with increasing temperature.

Seebeck coefficient represents changes in the energy of the carriers as they are excited into a higher state. In intrinsic semiconductors with a big gap, the Seebeck coefficient is large and typically display a T^{-1} relationship with temperature.[30] In metals or heavily-doped semiconductors, the Seebeck coefficient is small and increases with temperature.[30] For degenerate semiconductors, the Seebeck coefficient can be expressed mathematically[31] via the charge carrier concentration n, the effective mass $m*$, and temperature *T*.

$$\alpha = (\frac{8\pi^2 k_B^2}{3eh^2})m^* T(\frac{\pi}{3n})^{2/3} \quad (1\text{-}11)$$

It is worth pointing out that while the Seebeck coefficient is inversely related to the charge carrier concentration, the electrical conductivity is directly proportional to the carrier concentration. Furthermore, the effective mass m^* is inversely proportional to carrier mobility, μ, as heavier carriers tend to move slower. These trade-offs make the design of thermoelectric materials not a straightforward task, and optimizing the power factor is more like a compromising process. Generally, a carrier concentration in the range of 10^{19} to 10^{20} /cm^3 is favored[16], which is typical for heavily doped degenerate semiconductors. Such

carrier concentrations yield the desired Seebeck coefficient from 100 to 300 μVK^{-1} and electrical conductivity within 200 to 2000Scm^{-1}.

1.3.2 Reduction in Thermal Conductivity

A temperature gradient must be maintained for the charge carriers to create a potential difference (Seebeck voltage). Therefore, minimizing thermal conductivity is crucial to mitigate heat transfer between the hot end and the cold end.

The overall thermal conductivity, κ, is composed of the electrical thermal conductivity, κ_{el}, and lattice thermal conductivity, κ_l, describing the heat conduction by charge carriers and lattice vibration or phonons.

$$\kappa = \kappa_{el} + \kappa_l \tag{1-12}$$

One significant difficulty of thermoelectric material engineering is the linear relationship between the electrical thermal conductivity and electrical conductivity, expressed by the Wiedemann-Franz law[33], with L being the Lorenz number of 1.5-2.5$\times 10^{-8} V^2 K^{-2}$

$$k_{el} = L\sigma T \tag{1-13}$$

The lattice thermal conductivity is dependent on the specific heat capacity C_v, the speed of sound in the material v_s, and the phonon mean path l[33]:

$$K_l = \frac{1}{3} C_v v_s l \tag{1-14}$$

The phonon mean path tends to decrease at elevated temperatures, as increasing atomic vibrations scatter phonons and interfere with phonon propagation more frequently.[33] The speed of sound in the material depends on the density of material ρ, and Young's modulus Y, describing the rigidity of the lattice.

$$v_s = \sqrt{\frac{Y}{\rho}} \tag{1-15}$$

The specific heat capacity of the material is related to temperature T, molar gas constant R, and the Debye temperature θ_D , at which a solid exhibits maximal atomic vibrations.

$$C_v = 9R\left(\frac{T}{\theta_D}\right)^3 \int_0^{\frac{\theta_D}{T}} \frac{x^4 e^x}{(e^x-1)^2} dx \tag{1-16}$$

At high temperatures, the specific heat capacity no longer changes with the temperature and becomes constant, which is known as the Dulong-Petit law.[34] At high temperatures, T>>θ_D,

$$\int_0^{\frac{\theta_D}{T}} \frac{x^4 e^x}{(e^x-1)^2} dx \approx \frac{1}{3}(\frac{\theta_D}{T})^3 \tag{1-17}$$

Therefore,

$$C_v = 9R\left(\frac{T}{\theta_D}\right)^3 \frac{1}{3}\left(\frac{\theta_D}{T}\right)^3 = 3R \tag{1-18}$$

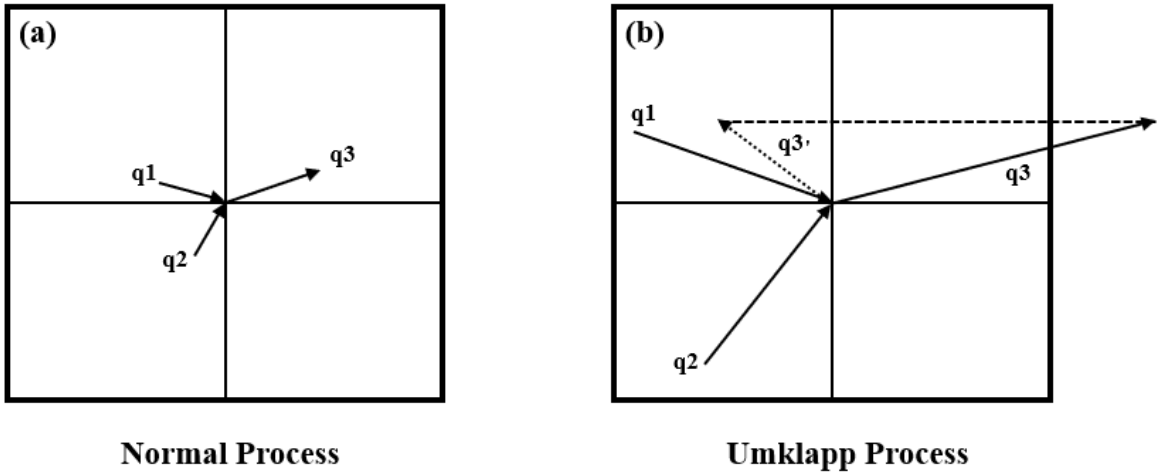

Figure 1.4. The summation of two wavevectors in the first Brillouin zone (a) The resulting vector is within the first Brillouin zone as a harmonic momentum conservation process. (b) The resulting vector extends outside the first Brillouin zone as an unharmonic Umklapp process.

Most solids experience an increasing specific heat capacity and lattice thermal conductivity with the rise of temperature, as more thermal energy induces more phonon propagation. Under low temperatures, phonons interact in a harmonic process where the momentum of wavevectors in the reciprocal space is conserved, and the atoms will vibrate normally. However, at some temperatures, the sum of wavevectors will extend outside of the first Brillouin zone. By definition, any point outside of the first Brillouin zone can be expressed as a point inside of it. Two wavevectors pointing to the right result in a sum vector pointing to the left, which can be interpreted as a violation of momentum conservation due to an unharmonic process. (Figure 1.4.) This phenomenon is called

Umklapp scattering; it occurs in high-temperature regions and displays a T^{-1} relationship for the lattice thermal conductivity.[29] Umklapp scattering is extensively beneficial to thermoelectric materials as it enhances the figure of merit zT by minimizing the lattice thermal conductivity.

Since the lattice thermal conductivity is not coupled to the charge transport, it can be tuned independently to enhance the overall thermoelectric efficiency. Some common strategies to minimize the lattice conductivity have focused on minimization of the mean free path of phonons, l, through doping and nanostructuring, and by using heavy elements to lower the speed of sound, v_s. Besides, structures with big unit cells are generally more favored than simple ones since the fraction of lattice vibrations that can carry heat is proportional to $N^{-\frac{2}{3}}$,with N being the number of atoms in one unit cell.[16] Additionally, phonons tend to scatter more often when the size difference between the neighboring atoms is significant[16]:

$$\frac{1}{l} \propto \frac{V}{4\pi v_s^3} \sum i f_i \left(\frac{m_{av} - m_i}{m_{av}}\right)^2 \qquad (1\text{-}19)$$

Here, V is the volume per atom, v_s is the speed of sound, f_i is the fraction of atoms with mass m_i, and m_{av} is the average mass of all atoms. Therefore, point defects and dopants

with significant differences in atomic masses are efficient ways to lower lattice thermal conductivity.

In conclusion, most solids can benefit from the Umklapp process and reach a minimal lattice thermal conductivity at high temperatures. At high temperatures, solids reach the constant specific heat capacity of $C_v = 3R$. Therefore, one can further simplify (1-14) to

$$K_l = \frac{1}{3}(3R)\sqrt{\frac{Y}{\rho}}l = R\sqrt{\frac{Y}{\rho}}l \qquad (1\text{-}20)$$

Thus, for a solid with heavy elements, soft chemical bonds, and an extremely short phonon mean free path similar to the interatomic separation, the lowest possible lattice thermal conductivity of 0.1-0.2 W $m^{-1}K^{-1}$ can be reached, and this value is referred to as the glass limit.[35] One well-agreed guideline for today's development of a successful thermoelectric material is to have a material that transports charge carriers like a crystal but scatters phonons like a glass. Such material is called a "phonon glass, electron crystal."[16]

1.4 Benchmarks of Thermoelectric materials

To better study and understand the strategies and challenges of thermoelectric engineering, it is worth reviewing some of the well-developed thermoelectric systems. A brief introduction of some benchmark thermoelectric systems is given in this section.

1.4.1 Strategies for Enhancing Thermoelectric Efficiency Today

Nanostructuring[36-38] introduces small nano-sized particles into the host domain, and this approach has been widely utilized for enhancing the Seebeck coefficient while lowering electrical conductivity and thermal conductivity. Nanoinclusions primarily increase grain boundaries and induce secondary phase scattering, leading to an ultra-low lattice thermal conductivity.[31,39]

Phonon wavelength varies in length; hence, a single implementation of a phonon-scatter source is insufficient. Hierarchical structure materials are the ones that have phonon-scattering constructions corresponding to all scales of wavelength. Point defects on the angstrom level are practical to scatter small wavelength phonons, while nanostructures such as a nano-secondary interface can scatter medium wavelength phonons; grain boundaries can scatter long wavelength phonons.[35] Hierarchical structures can drastically reduce lattice thermal conductivity.

Electronic band structure engineering via impurity phase or intramatrix band convergence has paved the way to preserve carrier mobility and power factor.[40-42] Band convergence takes advantage of the small difference in the conduction/valance bands between the host/impurity phases or different bands in the same phase. In the case of band convergence, carriers can transport across interfaces without scattering and can be

transported from both bands simultaneously. This process usually involves converging a flat heavy band with a large effective mass. Thermoelectric devices suffer low efficiency due to the inherent trade-off between electrical conductivity and the Seebeck coefficient. Energy filtering can alleviate this problem by stacking different layers of thermoelectric materials to pin up/down an energy barrier to filter out low-energy carriers and to allow only high-energy carriers to contribute to the physical properties of a material. In such a way, one can observe a substantial increase in the Seebeck coefficient and experience only a minor reduction in electrical conductivity.[43-45]

The aforementioned methods have played an essential role in optimizing thermoelectric performance and have successfully doubled the zT values. They served as guidelines for materials development and, on a personal level, in the author's experiments.

1.4.2 PbTe

PbTe-based materials are one of the most extensively studied thermoelectric systems. One reason is due to the affordable price and availability of raw materials. Most importantly, improvements from nanostructuring brought by secondary phase precipitations are substantial.[46] Nanostructuring can effectively enhance the charge carrier transport properties and suppress lattice phonon propagation. Well-studied systems such as $AgPb_mSbTe_{2+m}$ (LAST)[47], $Ag(Pb_{1-x}Sn_x)_mSbTe_{2+m}$ (TAGS)[48], and $NaPb_mSbTe_{2+m}$

(SALT)[49] show exemplary embedment of impurity phase and only slight lattice mismatch with the host phase. The well-embedded nano-sized phases preserve the host phase's electrical transport properties while drastically reducing the thermal conductivity. While efficiency hugely depends on the amount of the additional phases, studies show that the LAST-18 and SALT-20 reduce three-fold the thermal conductivity at room temperature compared to the host PbTe and achieve a peak zT of ~1.7 at 675-700K.[47,50,51]

1.4.3 SnTe

PbTe-based alloys have been studied as middle-temperature thermoelectric materials. However, due to lead's toxicity, an environment-friendly replacement is required. Similar to PbTe, SnTe processes the same rock salt structure and similar band structure[52]. However, SnTe suffers from 1) relatively high hole concentration induced by intrinsic Sn vacancies (>10^{21} cm^{-3}) originating from the lone pair effect[53]; 2) a small band gap which can induce severe bipolar conduction; 3) a large offset between the higher lying light hole band at the *L* point and the lower lying heavy hole band at the Σ point at room temperature (0.35eV). In comparison, the *L*- Σ offset in PbTe is only 0.17eV[54,55]. A larger offset in SnTe means the heavy hole band contributes less to charge transport in SnTe (*p*-type). As a result,

the Seebeck coefficient is lower, and electrical thermal conductivity, k_{el}, is higher, which leads to a zT value of only 0.5 at 873K for pristine SnTe[56].

Due to the similarity of atomic and electronic structures of SnTe and PbTe, techniques used for the optimization of PbTe can be applied to SnTe. The approaches include enhancement of the carrier transport via carrier concentration optimization[57, 58], band structure engineering through resonant states and band convergence[59, 60, 61], and lowering the thermal lattice conductivity by constructing all-scale hierarchical arvhitecture[59, 60, 61]. For instance, In dopants can sculpt the band structure of SnTe by forming resonant states in valence bands, thereby increasing the Seebeck coefficient[62]. Alternatively, Cd, Hg, and Mg alloying are reported to enhance the Seebeck coefficient via the convergence of the two valence bands[63, 64, 65]. Ways to reduce lattice thermal conductivity include the introduction of second phases, such as CdS, HgTe, and ZnS nanoprecipitates, which can strongly scatter heat-carrying phonons.[66] Recently, Tan reported that Mn alloying with its high solubility in SnTe (>13%) could also enhance the overall thermoelectric ability through valence band convergence.[67] Huang reported that the substitution of Ge for Sn in SnTe promotes the solubility of Mn in the SnTe phase, which enlarges the band gap and induces valence band convergence and thus leads to a higher Seebeck coefficient and better thermoelectric performance.[68]

1.4.4 GeTe

In contrast to PbTe and SnTe, which only crystalize with the NaCl structure at room temperature and above, GeTe undergoes a phase transition from low-temperature rhombohedral ($R3m$) to a high-temperature cubic ($Fm\bar{3}$m) around 720K.[69]

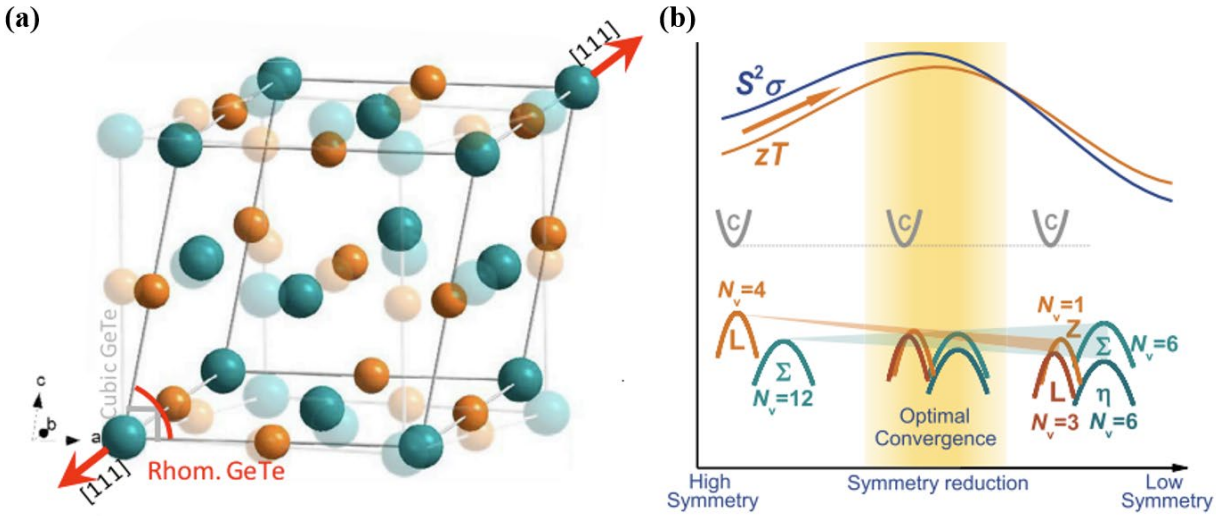

Figure 1.5 (a) a crystal structure of c-GeTe (shaded) and r-GeTe (colored) showing a distortion in the [111] direction. **(b)** a schematic diagram showing potential of a band convergence during the symmetry reduction.[69,74]

The rhombohedral GeTe (r-GeTe) can be visualized as the higher symmetry cubic GeTe (c-GeTe) distorted along the [1,1,1] direction.[69] This distortion originates from the Ge lone pair of the s electrons, which is involved in the strong hybridization of the Ge s orbital and Te p orbitals. Such strong hybridization causes uneven electron distribution and eventually leads to symmetry distortion.[70,71] As one can predict, c-GeTe has a band structure similar

to PbTe and SnTe. For c-GeTe, both the valence band maximum (VBM) and conduction band minimum (CBM) sit at the *L* point ($N_v = 4$) exhibiting a direct band gap. A secondary valence band sits lower than the *L* band along the ∑ direction ($N_v = 12$) with an energy offset ($\Delta E_{L-\Sigma}$) ~64meV.[72] While PbTe ($\Delta E_{L-\Sigma}$~100meV) and SnTe ($\Delta E_{L-\Sigma}$~300meV)[73] display good zT values at high temperatures due to the band convergence, c-GeTe with a smaller $\Delta E_{L-\Sigma} = 64$ meV performs even better at high temperatures. The cubic-to-rhombohedral phase change reduces the energy of the *L* band, resulting in the ∑ band now being the VBM. Moreover, this symmetry reduction to r-GeTe splits the 4L carrier pocket into 3L and 1Z, and the 12∑ into 6∑ and 6η.[74]

Due to the low formation energy of Ge vacancies originating from the lone pair effect, GeTe (p-type) is intrinsically off-stoichiometric and contains a large amount of Ge vacancies (Ge precipitation) leading to a hole concentration as high as ~10^{21} $cm^{-3,}$ significantly higher than its optimal level of ~2×10^{20} cm^{-3}.[75,76] Therefore, methodologies to suppress the excessive holes are the key to improving the GeTe materials. Such optimization methods include counter doping with group V elements (Sb, Bi, etc.) on the cation site[72,77]. An ideal carrier concentration level in GeTe would require heavy doping and alloying of ~10%, which may lead to significant compositional differences or changes in the band morphology. Besides, a high level of impurities can scatter phonons better,

resulting in a lower lattice thermal conductivity. Still, it can also interfere with carrier transport by reducing carrier mobility. Recent studies suggest that alloying with 1.5% of Cu_2Te [78] and self-compensation with 2% of Ge can successfully reduce the carrier concentration to the optimal level of $\sim 2 \times 10^{20}$ cm^{-3}. The introduction of Cu_2Te can drastically increase the formation energy of Ge vacancies. Both cases require only a small amount of dopant, preserving the composition and band structure well. It is worth noting that the lattice thermal conductivity in the r-GeTe is generally lower than that of the c-GeTe.[72] The reason is that the displacement of Ge atoms in r-GeTe distorts the octahedral bonds leading to three shorter bonds and three longer bonds between the Ge and Te atoms. The variation in bond length leads to variation in the inter-atom force constants. And the sound velocity is proportional to the square root of the geometric mean of the force constants.[79] Consequently, the asymmetrical bond length and asymmetrical interatomic forces in the r-GeTe lead to a lower sound velocity than in c-GeTe, which only has symmetrical bondings.[80]

1.4.5 Skutterutides

Skutterutides are another structure that has drawn much attention in the past decade and have become one of the most promising thermoelectric systems. Skutterudites are employed in space exploration missions due to their mechanical strength and chemical

robustness.[81] Their mechanical strength allows them to survive the stress from repeated thermal cycles, and the chemical stability provides freedom to optimize their electrical and thermal properties.

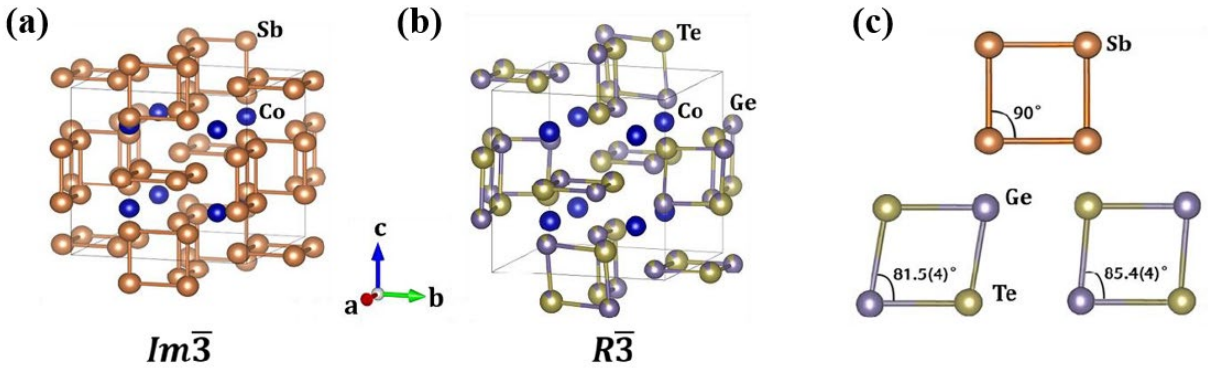

Figure 1.6. Crystal structure of (a) $CoSb_3$32 (space group $Im\bar{3}$) and (b) $CoGe_{1.5}Te_{1.5}$ (space group $R\bar{3}$). (c) A four-membered rectangular ring ($[Sb_4]^{4-}$) in $CoSb_3$ and two crystallographically distinct diamond-like rings ($[Ge_2Te_2]^{4-}$) in $CoGe_{1.5}Te_{1.5}$.

The traditional binary skutterudite, such as $CoSb_3$, possesses a cubic unit cell. The transition metal (M = Co) is intertwined with the square ring of covalently bonded pnictogen atoms (X_4 = Sb_4) in the directions of [1,0,0], [0,1,0], [0,0,1]. The transition metal sits in the center of the pnictogen octahedron.[82] Each pnictogen atom share two electrons with the neighboring pnictogens and needs only 1 extra electron to satisfy its octet rule. Herein, the charge balance limits the choices of the central transition metal to Co, Rh, Ir, when the anion is pnictogen (P, As, or Sb).[82] Compared to the binary skutterudites, ternary skutterudites exhibit lower lattice thermal conductivity. In filled ternary skutterudites, an

additional atom like a heavy lanthanoid occupies a large empty space and rattles inside this void. The rattling significantly suppresses the lattice thermal conductivity[83-88], while electrical conductivity can be optimized due to doping. In a mixed-anion ternary skutterudite like $CoGe_{1.5}S_{1.5}$, $CoSn_{1.5}Te_{1.5}$, and $CoGe_{1.5}Te_{1.5}$, the transition metal is surrounded by a near rectangular X-Y four-membered rings in a rhombohedral unit cell[82].

Chapter 2. Methodology and Characterization

2.1 X-ray Diffraction

2.1.1 X-ray Theory

X-ray diffraction is one of the most vital characterization techniques in Chemistry and Material Sciences. The process involved diffraction of the incident X-ray beam and detectition of the diffracted reflections. The diffracted data contains information about the composition and structure of the analyzed materials. For diffraction to occur, the sample needs to be crystalline; atoms need to be arranged in a periodic order. For a given structure and depending on the angle, the incident X-ray beam will be scattered by the electrons either destructively, which causes a systematic absence, or constructively. Bragg's law describes the relationship between the diffracted angle, θ, and interplanar distance, d_{hkl}, for a given wavelength, λ:

$$n\lambda = 2d_{hkl}sin\theta \quad (2\text{-}1)$$

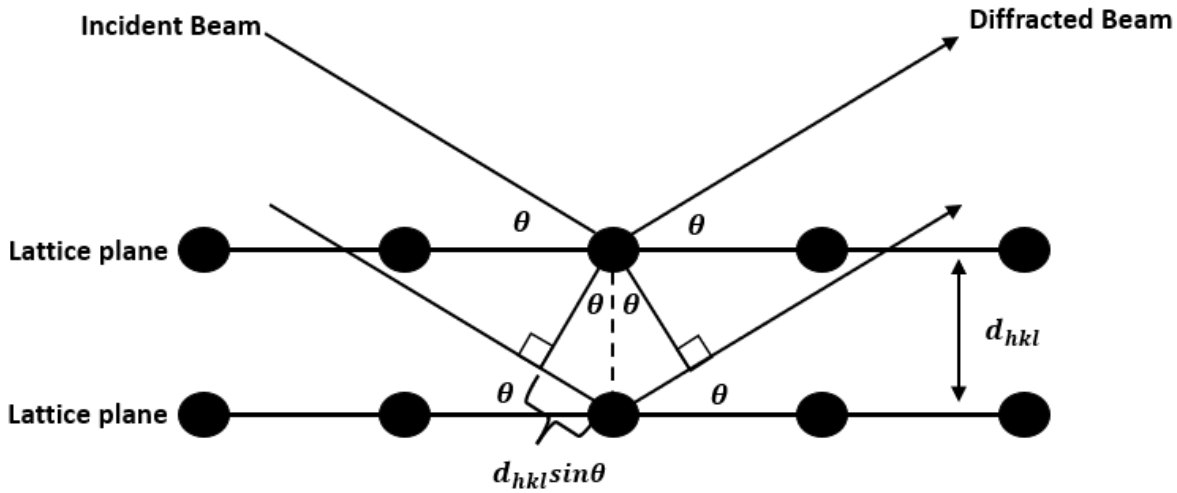

Figure2.1 A scenario of the X-ray beam diffracted by the periodic lattice. When the path difference between the two beams ($2d_{hkl}sin\theta$) is equal to the multiple of the incident beam wavelength; a constructive interference happens, and a signal is detected.

The smallest repeating unit or the building block of a crystalline solid is called a unit cell, which can be described by the basic vectors, *a, b, c*, and the angles *α, β, and γ*. One can further relate the (*h,k,l*) Miller indices for a given (*h,k,l*) plane to the unit cell parameters by describing how many times the unit cell is divided by these lattice planes along each direction. It is convenient to analyze the diffraction in the reciprocal space. The reciprocal unit cell is described by the reciprocal vectors a^*, b^*, and c^*, which are the cross product of the other two vectors in the real space divided by the cell volume *V*.

$$a^* = \frac{b \times c}{V}, b^* = \frac{a \times c}{V}, c^* = \frac{a \times b}{V} \quad (2\text{-}2)$$

Any (*h,k,l*) plane in the real space can be expressed by a normal in the reciprocal space with an absolute value $d^* = 1/d$, which can be related to a linear combination of $a^*, b^*$and c^*

$$d^* = ha^* + kb^* + lc^* \tag{2-3}$$

Paul Peter Ewald used the reciprocal space to visualize the diffraction events in the 1920s[89]. He constructed a sphere with a radius of $\frac{1}{\lambda}$, which is now called an Ewald's sphere (Figure 2.2.). The origin of the reciprocal lattice is at point O on the Ewald's sphere. The incoming X-ray beam is represented by the reciprocal CO vector, and the diffracted beam by the CP vector, both of which are $\frac{1}{\lambda}$ long. The angle between the incoming and diffracted beams is θ. It can be shown if a (*hkl*) reciprocal lattice point with *d** touches the surface of the sphere, then the diffraction event occurs; that is the Brag's law is satisfied.

$$d^* = \frac{1}{d} \tag{2-4}$$

$$sin\theta = \frac{OP/2}{CO} == \frac{d^*/2}{\frac{1}{\lambda}} = \frac{\lambda}{2d} \quad \Rightarrow \quad 2dsin\theta = \lambda \tag{2-5}$$

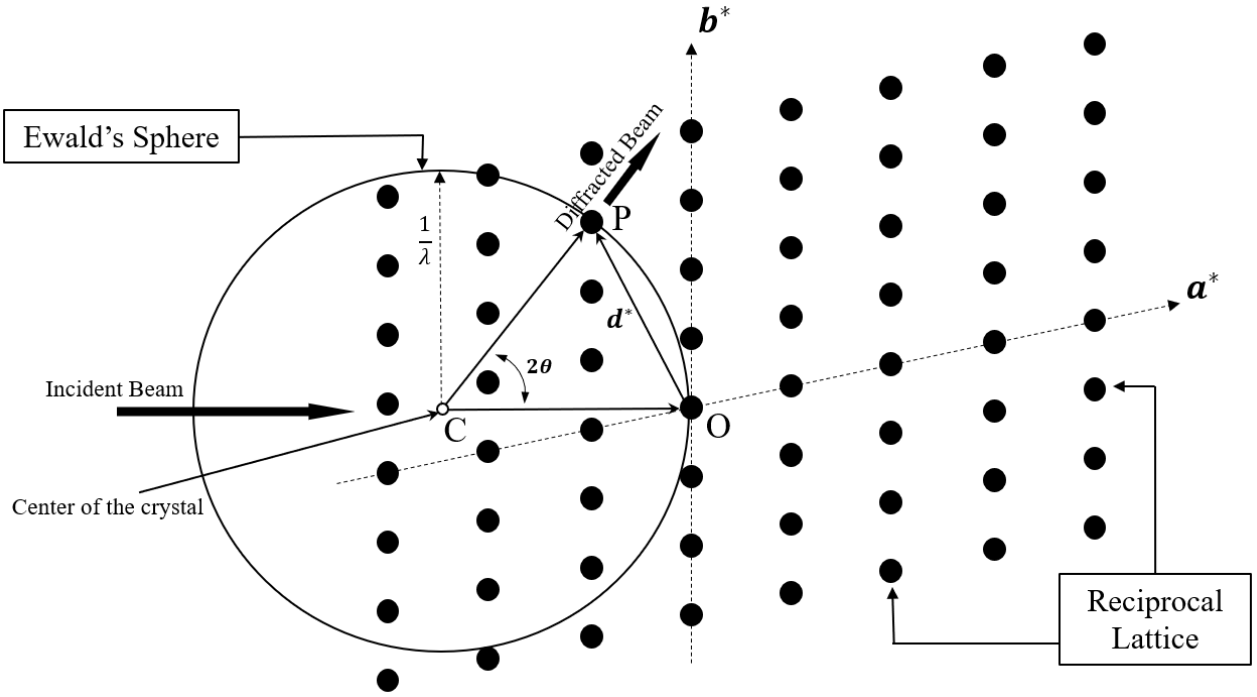

Figure2.2 A demonstration of the Ewald sphere showing a relationship between the incident X-ray beam and Bragg's law in the reciprocal space.

The atomic scattering factor *f* describes how well an atom scatters X-rays. Generally, larger atoms with more electrons tend to diffract better due to their larger numbers of electrons. In contrast, the atomic scattering factor is inversely proportional to the diffraction angle due to the increased destructive interference caused by an increased path difference.

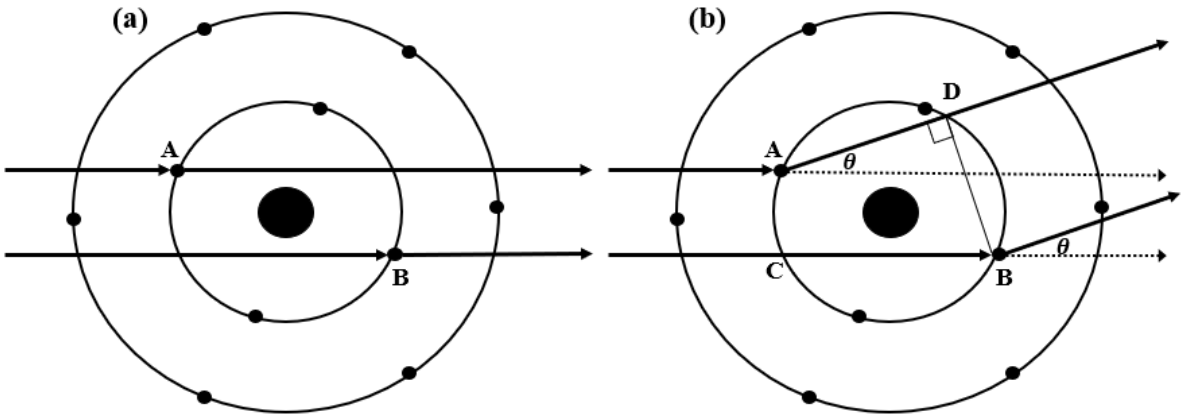

Figure2.3 (a) The path difference is equal to 0 when the diffraction angle θ is 0°. **(b)** A path difference is introduced with a length of $BC - AD$ when the diffraction angle θ is greater than 0°.

When the diffraction angle θ is 0°, there is no difference in the path between the two beams (Figure 2.3). However, when θ is larger than 0°, a path difference with a length of $CB - AD$ is introduced, and it will increase with θ resulting in more destructive interference. This effect will be more pronounced for smaller wavelength X-rays. Thus, the atomic scattering factor is a function of $\frac{sin\theta}{\lambda}$ or the reciprocal interplanar distance, since $\frac{sin\theta}{\lambda} = \frac{1}{2d}$, which is independent of the λ. However, this is only true for light elements and short wavelengths. In reality, most of the atoms scatter X-rays anomalously.[90]

$$f_{j(s)} = f_{j0}(s) + \Delta f_j' + i\Delta f_j'' \qquad (2\text{-}6)$$

$f_{j0}(s)$ is a function of $\frac{sin\theta}{\lambda}$. The real and imaginary parts account for anomalous scattering, which is dependent on the atoms and the wavelength.[84] The magnitude of the anomalous scattering is proportional to the wavelength and inversely proportional to the number of electrons in the atoms. The magnitude of the anomalous scattering is at least one order smaller than the normal scattering. It reaches its peak when the wavelength is close to the absorption edge of the atom.[90]

A structure factor contains all the information about a diffraction plane, including intensity and phase angle, which depends on the type and positions of atoms in a crystal structure. Due to the periodicity of a crystal, a structure factor for a reflection is expressed as a Fourier series of an atomic scattering factor and atomic positions inside the unit cell.[91]

$$F_{hkl} = \sum_{j=1}^{n} g_j f_j(s) t_j(s) \exp\left[2\pi i\left(hx_j + ky_j + lz_j\right)\right] \quad (2\text{-}7)$$

g_j is the population factor of the *j*th atom, t_j is the atomic displacement parameter describing displacements of the *j*th atom.[90] The exponential part can be expressed as an Euler expansion of sin and cos terms with a phase angle $\varphi = 2\pi(hx_n + ky_n + lz_n)$.

$$e^{2\pi i(hx_j+ky_j+lz_j)} = cos2\pi\left(hx_j + ky_j + lz_j\right) + isin2\pi(hx_j + ky_j + lz_j) \quad (2\text{-}8)$$

One can gather intensity information experimentally, and it is proportional to $|F_{hkl}|^2$. Unfortunately, neither $|F_{hkl}|$ nor $|F_{hkl}|^2$ contain information regarding the phase angle

which is required to locate the atoms inside the unit cell. A direct method includes repetitive attempts to assign initial phase angles to a few reflections and expand the number of phase angles through the triple relationship. Based on the statistical analysis, correct phase angles are identified, and a structural solution is obtained by this process.[92] Before the direct methods are applied, the space group is determined based on the systematic absence in the diffraction pattern. The systematic absence stems from symmetry elements with translational symmetry.[90]

2.1.2 X-ray Powder Diffraction

Although single crystal X-ray diffraction offers extraordinary information regarding the atomic structure, it requires crystals of suitable size and may not represent the bulk of a material. For thermoelectric material studies, it is vital to have a fast and robust method to examine the bulk material. Herein, X-ray powder diffraction is utilized to check the phases and purity in the author's thermoelectric projects.

The sample is finely ground for powder diffraction, and the one-dimensional powder diffraction pattern is recorded. The obtained pattern allows researchers to identify the phases and assess the purity of the samples.

Both the GeTe and the skutterudite phases presented in this thesis paper were analyzed on a PANalytical X'Pert Pro diffractometer with a one-dimensional X'Celerator detector. The X-ray source was the Cu Kα_1 radiaion, a Ge monochromator was used to eliminate undesired Cu Kα_2. A silicon single crystal plate cut parallel to the (510) plane was used as a sample holder as it contributes no Bragg peaks during diffraction.[93]

2.2 Energy Dispersive X-ray Spectroscopy

X-ray diffraction has certain limitations, such as elements with similar electron counts cannot be distinguished, and impurities that are amorphous or in small amounts may not be detected. In such cases, scanning electron microscopy (SEM) coupled with energy dispersive X-ray spectroscopy (EDS or EDX) is used. During the EDS analysis, the incoming electron beam knocks off a core electron in the atom, leaving a hole. A higher energy state electron will relax to the lower state and replace the ejected electron emitting a characteristic X-ray photon specific to the element. By analyzing the X-ray spectrum, the sample's elemental composition can be determined.[94].

2.3 Hall Effect Measurement

As described in Chapter 1.4.4, GeTe materials possess a high hole concentration, which leads to an inferior figure of merit *zT*. Therefore, a method that can allow us to measure the carrier concentration is vital for thermoelectric engineering.

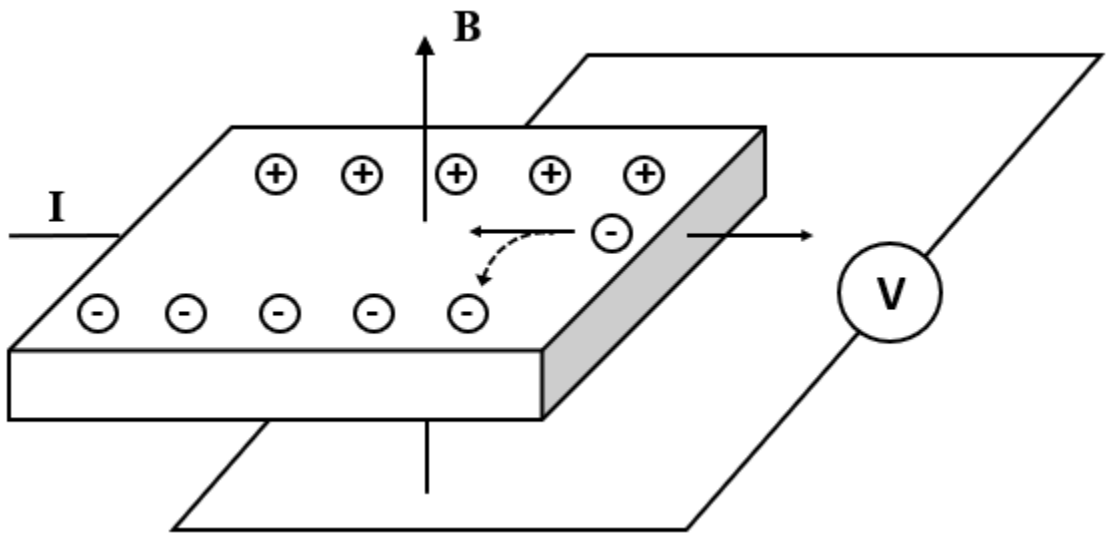

Figure2.4 A schematic diagram of the Hall effect. A current I passes through the x-direction with an applied magnetic field in the y-direction. The charge carrier (electron in the diagram; opposite the direction of the current) propagates in a curved direction affected by the Lorentz force, resulting in a voltage in the z-direction.

The charge carriers in the electrical field move in a straight path. However, when a perpendicular magnetic field is applied, the Lorentz force will deviate from the moving charge carriers. This will result in a voltage perpendicular to both the direction of the current and the magnetic field.[95] The Hall coefficient is defined as,

$$R_H = \frac{E_y}{j_x B_z} \tag{2-9}$$

where E is the induced electric field, j is the current density, B is the magnetic field.

For semiconductors, the conduction can be contributed simultaneously by electrons and holes, which may be in different concentrations and have different mobility.[96]

$$R_H = \frac{p\mu_h^2 - n\mu_e^2}{e(p\mu_h - n\mu_e)^2} \tag{2-10}$$

where n is the electron concentration, p is the hole concentration, μ_e is the electron mobility, μ_h is the hole mobility, and e is the elementary charge.

References

1. Disalvo, F. J., *Science (Washington, D. C.)* **1999,** *285* (5428), 703-706.
2. Tritt, T. M., *Science (Washington, D. C.)* **1996,** *272* (5266), 1276-1277.
3. Seebeck, T. J., *Treatises of the Royal Academy of Sciences in Berlin* **1825**, 265-373.
4. Ørsted, H. C., *Annales de Chimie et Physique 22* **1823**, 375–389.
5. Lasance, C. J. M., *Electronics Cooling* **2006,** (November).
6. Winder, E. J.; Ellis, A. B.; Lisensky, G. C., *J. Chem. Educ.* **1996,** *73* (10), 940-946.
7. Fermi, E., Rendiconti Lincei 1926, 3, 145-149.
8. Dirac, P. A. M., Proceedings of the Royal Society, Series A 1926, 112 (762), 661-677.
9. Bloch, F., *Z. Physik* **1928,** *52*, 555-600.
10. Kittel, C., *Introduction to Solid State Physics* **2005,** *8th Ed.*, 194-196.
11. Rowe, D. M., *CRC Handbook of Thermoelectrics: Macro to Nano* **2005**, CRC Press.
12. Lenz, H. F. E., *Ann. Electr. II.* **1839**, 380-384.
13. Sittig, M., *Thermoelectric materials* **1970**, Noyes Data Corp.
14. William, T., *R. Soc. Edinburgh: Earth Sci.* **1851,** *3*, 91–98.
15. Ioffe, A. F., *Semiconductor Thermoelements and Thermoelectric Cooling* **1957**, London, Infosearch.
16. Rowe, D. M., *CRC Handbook of Thermoelectrics* **1995**, CRC Press.
17. Heikes, R. R.; Ur, R. W., *Interscience Publishers* **1961**.
18. Cadoff, I. B.; Miller, E., *Materials Technology Series. Reinhold Publishing Cooperation* **1960**.
19. Egli, P. H., *John Wiley & Sons* **1960**.
20. Snyder, G. J., *Appl. Phys. Lett.* **2004,** *84* (13), 2436-2438.
21. Snyder, G. J.; Ursell, T. S., *Phys. Rev. Lett.* **2003,** *91* (14), 148301:1-148301:4.
22. Perpetua, *http://www.perpetuapower.com/index.htm*.
23. Caframo, *http://www.caframolifestylesolutions.com/*.
24. Powerpractical, *http://powerpractical.com/*.
25. Yang, J.; Caillat, T., *MRS Bull.* **2006,** *31* (3), 224-229.
26. Cook, J. C.; Agle, D. C.; D., B., *NASA Voyager mission, NASA* **2013**.
27. Sootsman, J. R.; Chung, D. Y.; Kanatzidis, M. G., *Angew. Chem., Int. Ed.* **2009,** *48* (46), 8616-8639.
28. MacDonald, D. K. C., *Thermoelectricity: An Introduction to the Principles* **1962**, John Wiley & Sons, Inc.
29. Omar, M. A., *Elementary Solid State Physics: Principles and Applications* **1999**, Pearson Education, Inc.
30. Cutler, M.; Mott, N. F., *Phys. Rev.* **1969,** *181* (3), 1336-1340.
31. Snyder, G. J.; Toberer, E. S., *Nat. Mater.* **2008,** *7* (2), 105-114.
32. Jonson, M.; Mahan, G. D., *Phys. Rev. B* **1980,** *21* (10), 4223-9.
33. White, M. A., *Properties of Materials* **1999**, Oxford University Press: New York.
34. Petit, A.-T.; Dulong, P.-L., *Annales de Chimie et de Physique* **1819,** *10*, 395-413.
35. Biswas, K.; He, J.; Blum, I. D.; Wu, C.-I.; Hogan, T. P.; Seidman, D. N.; Dravid, V. P.; Kanatzidis, M. G., *Nature (London, U. K.)* **2012,** *489* (7416), 414-418.
36. Balandin, A.; Wang, K. L., *J. Appl. Phys.* **1998,** *84* (11), 6149-6153.
37. Hicks, L. D.; Dresselhaus, M. S., *Phys. Rev. B* **1993,** *47* (19), 12727-12731.

38. Hicks, L. D.; Harman, T. C.; Dresselhaus, T. C., *Appl. Phys. Lett.* **1993,** *63* (23), 3230-3232.
39. Minnich, A. J.; Dresselhaus, M. S.; Ren, Z. F.; Chen, G., *Energy Environ. Sci.* **2009,** *2* (5), 466-479.
40. Heinrich, H.; Lischka, K.; Sitter, H.; Kriechbaum, M., *Phys. Rev. Lett.* **1975,** *35* (16), 1107-1110.
41. Zhao, L.-D.; Hao, S.; Lo, S.-H.; Wu, C.-I.; Zhou, X.; Lee, Y.; Li, H.; Biswas, K.; Hogan, T. P.; Uher, C.; Wolverton, C.; Dravid, V. P.; Kanatzidis, M. G., *J. Am. Chem. Soc.* **2013,** *135* (19), 7364-7370.
42. Zhao, L.-D.; He, J.; Hao, S.; Wu, C.-I.; Hogan, T. P.; Wolverton, C.; Dravid, V. P.; Kanatzidis, M. G., *J. Am. Chem. Soc.* **2012,** *134* (39), 16327-16336.
43. Bulat, L. P.; Drabkin, I. A.; Karataev, V. V.; Osvenskii, V. B.; Parkhomenko, Y. N.; Pshenai-Severin, D. A.; Pivovarov, G. I.; Tabachkova, N. Y., *Phys. Solid State* **2011,** *53* (1), 29-34.
44. Zide, J. M. O.; Vashaee, D.; Bian, Z. X.; Zeng, G.; Bowers, J. E.; Shakouri, A.; Gossard, A. C., *Phys. Rev. B* **2006,** *74* (20), 205335:1-205335:5.
45. Zide, J. M. O.; Vashaee, D.; Zeng, G.; Bowers, J. E.; Shakouri, A.; Gossard, A. C., *Los Alamos Natl. Lab., Prepr. Arch.* **2005**, 1-18.
46. Forbes, S. H. *Investigation and Characterization of Rare-Earth Pnictide Suboxides for Thermoelectric Applications*. Thesis, **2015**, pp 25–25.
47. Quarez, E.; Hsu, K.-F.; Pcionek, R.; Frangis, N.; Polychroniadis, E. K.; Kanatzidis, M. G., *J. Am. Chem. Soc.* **2005,** *127* (25), 9177-9190.
48. Androulakis, J.; Pcionek, R.; Quarez, E.; Palchik, O.; Kong, H.; Uher, C.; Dangelo, J. J.; Hogan, T.; Tang, X.; Tritt, T.; Kanatzidis, M. G., *Mater. Res. Soc. Symp. Proc.* **2006,** *886* (Materials and Technologies for Direct Thermal-to-Electric Energy Conversion), 187-194.
49. Poudeu, P. F. P.; D'Angelo, J.; Downey, A. D.; Short, J. L.; Hogan, T. P.; Kanatzidis, M. G., *Angew. Chem., Int. Ed.* **2006,** *45* (23), 3835-3839.
50. Cook, B. A.; Kramer, M. J.; Harringa, J. L.; Han, M.-K.; Chung, D.-Y.; Kanatzidis, M. G., *Advanced Functional Materials* **2009,** *19* (8), 1254-1259.
51. Hsu, K. F.; Loo, S.; Guo, F.; Chen, W.; Dyck, J. S.; Uher, C.; Hogan, T.; Polychroniadis, E. K.; Kanatzidis, M. G., *Science (Washington, DC, U. S.)* **2004,** *303* (5659), 818-821.
52. W. Li, Y. Wu, S. Lin, Z. Chen, J. Li, X. ZW. Li, Y. Wu, S. Lin, Z. Chen, J. Li, X. Zhang, L. Zheng, Y. Pei, *ACS Energy Lett*. 2017, 2, 2349hang, L. Zheng, Y. Pei, ACS Energy Lett. 2017, 2, 2349
53. a) R. Brebrick, J. *Phys. Chem. Solids* 1963, 24, 27; b) R. F. Brebrick, A. J. Strauss, *Phys. Rev*. 1963, 132, 2800.
54. R. F. Brebrick and A. J. Strauss, *Anomalous thermoelectricpower as evidence for two-valence bands in SnTe, Phys. Rev*.,1963, 131(1), 104.
55. L. M. Rogers, *Valence band structure of SnTe, J. Phys. D:Appl. Phys*., 1968, 1(7), 845.
56. H. Wu, C. Chang, D. Feng, Y. Xiao, X. Zhang, Y. Pei, L. Zheng, D. Wu, S. Gong, Y. Chen, *Energy Environ. Sci.* 2015, 8, 3298.

57. 1 Y. Pei, A. D. LaLonde, N. A. Heinz, X. Shi, S. Iwanaga, H. Wang, L. Chen and G. J. Snyder, *Adv. Mater*., 2011, 23, 5674–5678.
58. H. Wang, Y. Pei, A. D. LaLonde and G. J. Snyder, *Adv. Mater*., 2011, 23, 1366–1370.
59. Y. Pei, X. Shi, A. LaLonde, H. Wang, L. Chen and G. J. Snyder, *Nature*, 2011, 473, 66–69.
60. 4 H. J. Wu, L. D. Zhao, F. S. Zheng, D. Wu, Y. L. Pei, X. Tong, M. G. Kanatzidis and J. Q. He, *Nat. Commun*., 2014, 5, 4515.
61. L. D. Zhao, H. J. Wu, S. Q. Hao, C. I. Wu, X. Y. Zhou, K. Biswas, J. Q. He, T. P. Hogan, C. Uher, C. Wolverton, V. P. Dravid and M. G. Kanatzidis, *Energy Environ. Sci*., 2013, 6, 3346–3355.
62. Q. Zhang, B. Liao, Y. Lan, K. Lukas, W. Liu, K. Esfarjani, C. Opeil, D. Broido, G. Chen and Z. Ren, Proc. *Natl. Acad. Sci*. U. S. A., 2013, 110, 13261–13266.
63. 1 G. Tan, L.-D. Zhao, F. Shi, J. W. Doak, S.-H. Lo, H. Sun, C. Wolverton, V. P. Dravid, C. Uher and M. G. Kanatzidis, J. *Am. Chem. Soc*., 2014, 136, 7006–7017.
64. G. Tan, F. Shi, J. W. Doak, H. Sun, L.-D. Zhao, P. Wang, C. Uher, C. Wolverton, V. P. Dravid and M. G. Kanatzidis, *Energy Environ. Sci*., 2015, 8, 267–277.
65. A. Banik, U. S. Shenoy, S. Anand, U. V. Waghmare and K. Biswas, *Chem. Mater*., 2015, 27, 581–587.
66. G. Tan, F. Shi, S. Hao, H. Chi, L.-D. Zhao, C. Uher, C. Wolverton, V. P. Dravid and M. G. Kanatzidis, J. *Am. Chem. Soc*., 2015, 137, 5100–5112.
67. G. Tan, F. Shi, S. Hao, H. Chi, T. P. Bailey, L.-D. Zhao, C. Uher, C. Wolverton, V. P. Dravid and M. G. Kanatzidis, J. *Am. Chem. Soc*., 2015, 137, 11507–11516.
68. Li, J. Q., Huang, S., Chen, Z. P., Li, Y., Song, S. H., Liu, F. S., and Ao, W. Q. (2017) *Phases and thermoelectric properties of SNTE with (Ge, Mn) co-doping. Physical Chemistry Chemical Physics* 19, 28749–28755.
69. Chattopadhyay, T., Boucherle, J.X., and Schnering, H.G. (1987). *Neutron diffraction study on the structural phase transition in GeTe. J. Phys. C Solid State Phys*. 20, 1431–1440.
70. Waghmare, U.V., Spaldin, N.A., Kandpal, H.C., and Seshadri, R. (2003). *First-principles indicators of metallicity and cation offcentricity in the IV-VI rocksalt chalcogenides of divalent Ge, Sn, and Pb. Phys. Rev.* B 67, 125111.
71. Zeier, W.G., Zevalkink, A., Gibbs, Z.M., Hautier, G., Kanatzidis, M.G., and Snyder, G.J. (2016). *Thinking like a chemist-intuition in thermoelectric materials. Angew. Chem. Int. Ed. Engl.* 55, 6826–6841.
72. Li, J., Chen, Z., Zhang, X., Sun, Y., Yang, J., and Pei, Y. (2017). *Electronic origin of the high thermoelectric performance of GeTe among the p-type group IV monotellurides. NPG Asia Mater* 9, e353.
73. Tung, Y.W., and Cohen, M.L. (1969). *Relativistic band structure and electronic properties of SnTe, GeTe, and PbTe. Phys. Rev.* 180, 823–826.
74. Li, J., Zhang, X., Chen, Z., Lin, S., Li, W., Shen, J., Witting, I.T., Faghaninia, A., Chen, Y., Jain, A., et al. (2018). *Low-symmetry rhombohedral GeTe thermoelectrics. Joule 2*, 976–987.

75. Li, J., Chen, Z., Zhang, X., Yu, H., Wu, Z., Xie, H., Chen, Y., and Pei, Y. (2017). *Simultaneous optimization of carrier concentration and alloy scattering for ultrahigh performance GeTe thermoelectrics. Adv. Sci*. 4, 1700341.
76. Zhang, X., Li, J., Wang, X., Chen, Z., Mao, J., Chen, Y., and Pei, Y. (2018). *Vacancy manipulation for thermoelectric enhancements in GeTe alloys. J. Am. Chem. Soc.* 140, 15883–15888.
77. Perumal, S., Roychowdhury, S., Negi, D.S., Datta, R., and Biswas, K. (2015). *High thermoelectric performance and enhanced mechanical stability of p-type Ge1–xSbxTe. Chem. Mater.* 27, 7171–7178.
78. Bu, Z., Li, W., Li, J., Zhang, X., Mao, J., Chen, Y., and Pei, Y. (2019). *Dilute Cu_2Te alloying enables extraordinary performance of r-GeTe thermoelectrics. Mater. Today Phys. 9*, 100096.79. Zhang, X.; Bu, Z.; Lin, S.; Chen, Z.; Li, W.; Pei, Y. *GeTe Thermoelectrics. Joule* 2020, 4 (5), 986–1003.
80. Chen, Z.W., Zhang, X.Y., Lin, S.Q., Chen, L.D., and Pei, Y.Z. (2018). *Rationalizing phonon dispersion for lattice thermal conductivity of solids. Natl. Sci. Rev.* 5, 888–894.
81. 5J. P. Fleurial, T. Caillat, and A. Borshchevsky, in *Proceedings of the 17th International Conference on Thermoelectrics*, ICT97 (IEEE, New York, 1997), pp. 1–11.
82. Volja, D.; Kozinsky, B.; Li, A.; Wee, D.; Marzari, N.; Fornari, M. *Electronic, Vibrational, and Transport Properties of Pnictogen-Substituted Ternary Skutterudites. Physical Review B* 2012, 85 (24).
83. Fleurial, J.-P.; Borshchevsky, A.; Caillat, T.; Morelli, D. T.; Meisner, G. P. *High Figure of Merit in CE-Filled Skutterudites*. *Fifteenth International Conference on Thermoelectrics. Proceedings ICT '96*.
84. Jeitschko, W.; Braun, D. *LaFe4P12 With Filled CoAs3-Type Structure and Isotypic Lanthanoid-Transition Metal Polyphosphides*. *Acta Crystallographica Section B Structural Crystallography and Crystal Chemistry* **1977**, *33* (11), 3401–3406.
85. Li, W.; Mingo, N. *Thermal Conductivity of Fully Filled Skutterudites: Role of the Filler. Physical Review B* **2014**, *89* (18).
86. Sales, B. C.; Mandrus, D.; Chakoumakos, B. C.; Keppens, V.; Thompson, J. R. *Filled Skutterudite Antimonides: Electron Crystals and Phonon Glasses. Physical Review B* **1997**, *56* (23), 15081–15089.
87. Sales, B. C.; Mandrus, D.; Williams, R. K. *Filled Skutterudite Antimonides: A New Class of Thermoelectric Materials*. *Science* **1996**, *272* (5266), 1325–1328.
88. Shi, X.; Yang, J.; Salvador, J. R.; Chi, M.; Cho, J. Y.; Wang, H.; Bai, S.; Yang, J.; Zhang, W.; Chen, L. *Multiple-Filled Skutterudites: High Thermoelectric Figure of Merit through Separately Optimizing Electrical and Thermal Transports*. *Journal of the American Chemical Society* **2011**, *133* (20), 7837–7846.
89. Ewald, P. P. Die Berechnung Optischer Und Elektrostatischer Gitterpotentiale. *Annalen der Physik* **1921**, *369* (3), 253–287.
90. Mozharivskyj, Y. Structure factor. *X-ray theory*, 2020.
91. Cullity, B. D., *Elements of X-Ray Diffraction* **1967**, Addison-Wesley Publishing Company, Inc.
92. Palmer, M. F. C., *Structure Determination by X-ray Crystallography 3rd ed.* **1993**, Pleum Press.

93. Mozharivskyj, Y. Diffraction Techniques. *X-ray theory*, 2020.
94. Egerton, R. F., *Physical Principles of Electron Microscopy: an Introduction to TEM, SEM, and AEM* **2005**, Springer Science & Business Media.
95. Hall, E., *American Journal of Mathematics* **1879,** *2* (3), 287-292.
96. Kasap, S. O. *Hall effect in semiconductors*; s.n.: S.l., 2001.

Chapter 3. ZnO Induces Ge Self-Compensation and Enhances Thermoelectric Performance of GeTe

This chapter is based on the manuscript of "ZnO Induces Ge Self-Compensation and Enhances Thermoelectric Performance of GeTe." Yuyang Huang and Zan Yang carried out the experimental procedure and analysis of the data. Dr. Yu-Chih Tseng helped with the property measurements and Ph.D. candidate Evan Smith's electronic band calculations.

3.1 Introduction

Thermoelectric materials have received extensive attention in recent years due to their ability to directly convert waste heat into electricity and owing to the global energy crisis. The performance of a thermoelectric device is governed by a dimensionless figure of merit zT value, $zT = \frac{S^2\sigma}{\kappa_l + k_e}T$, where S, σ, κ_l, k_e, and T are Seebeck coefficient, electrical conductivity, lattice and electronic thermal conductivity, and absolute temperature, respectively. Since S, σ, and κ_e are intrinsically coupled with each other, their simultaneous optimization is a complex and subtle task. Extraordinary progress has been made in the last 10 years, by employing band structure optimization[1–5], nanostructure engineering[6–10], high entropy alloying[11–18], and as a result, the zT values above 2 at 800K are now achieved.

Among numerous thermoelectric systems, PbTe[19–25] and SnSe[26–34] are considered to be the most promising candidates for mid-temperature (300K ~ 800K) energy harvesting. Recent breakthroughs on the polycrystalline SnSe even set a record of a peak *zT* of 3.1 at 783K[35]. Despite the attractive performance, the high fabrication cost of SnSe and the toxic nature of PbTe prevent them from widespread applications. GeTe, an analogue of PbTe, has also attracted much attention in the last few years[2,4,36–46]. By properly optimizing the carrier concentration and band structure, the performance of GeTe could be comparable with that of the PbTe-based materials.

Elemental doping was extensively studied both experimentally and computationally, and remarkable progress has been achieved [7,38,47–50]. However, most high-performance materials include rare elements or toxic metals. In this work, the possibility of improving the thermoelectric performance of GeTe via doping with ZnO nanoparticles was explored. It was found that the introduction of nanosized ZnO increased the Seebeck coefficient while its electrical conductivity was maintained at a reasonable level, which resulted in a substantial enhancement of the power factor. A peak *zT* of 1.73 at 672K and an average *zT* of 0.91 for 323K ~ 733K were achieved, which corresponds to 29% and 42% improvement over the pristine GeTe, respectively. This work demonstrates the potential of ZnO as an effective eco-friendly dopant in the GeTe and potentially other systems.

3.2 Experimental Methods

Sample preparation: GeTe + *x wt.*% ZnO (*x* = 0, 0.5, 1.0, 1.5) samples were synthesised via two-step process. Ge (pieces, 99.999 wt.%), Te (lump, 99.999 wt.%) were weighted according to the stoichiometric ratios and loaded into the silica tubes. After evacuation, the tubes were sealed by an oxygen/natural gas torch. Samples were then heated to 1000 ℃ for 12h and kept for 12h before being quenched in ice water. The obtained ingots were then hand grounded with pestle and mortar for 1h inside an argon glovebox and then sealed inside a Teflon ball milling jar. Powders were ball milled at 200rpm for 2h using a Fritsch PULVERISETTE 6 planetary ball milling machine. The obtained powders were mixed with *x wt.*% (*x* = 0, 0.5, 1.0, 1.5) of nanosized ZnO powders (⩽100 nm) via ball milling under 200rpm for 15min. The mixed powders were then densified by spark plasma sintering (SPS) in a graphite die with a diameter of 15 mm. During the sintering, powders were heated to 400 ℃ and held for 5 min under a pressure of 40 MPa.

Phase identification: Powder X-ray diffraction (PXRD) data were collected in the range of 2θ= 20-120° on a PANalytical X'Pert Pro diffractometer equipped with a linear X'Celerator detector and using $CuK_{\alpha 1}$ (λ = 1.5406 Å) radiation at room temperature. For

the analysis, the sintered samples were grounded into fine powders and deposited on a zero-background silicon disc.

Thermoelectric properties characterization: Simultaneous data collection of the Seebeck coefficient and electrical resistivity was performed under a helium atmosphere in a range of 300 - 750K on a ULVAC-RIKO ZEM-3 instrument. Samples were cut into 2 x 2 x 8 mm^3 bars for high-temperature transport property measurements (σ, S). The total thermal conductivity, κ, was calculated using the formula $\kappa = DC_p\rho$, where ρ is the sample density, measured by the Archimedes method with all samples showing a high relative density of over 95%. Thermal diffusivity D was measured in the range of 300 to 800K using laser flash diffusivity (LFA) method on a Netzsch LFA-457 instrument. Samples with a dimension of 10×10×1.5 mm^3 squares were used for LFA. Heat capacity C_p was estimated from the Dulong-Petit law.

Microstructure Analysis: Microstructural analysis was performed on a scanning electron microscopy (SEM, JEOL JSM-7000F, JP) in both secondary and backscatter modes of imaging. Elemental distribution was determined via energy dispersive X-ray spectroscopy (EDS).

Theoretical calculations: Electronic structure calculations were performed with the density functional theory via the Quantum Espresso[51,52]. A projector-augmented wave (PAW) technique was chosen to model the electron-ion interaction for the Ge and Te atoms. The parameterization by Predew, Burke and Ernzerfhof (PBE) based on generalized gradient approximation (GGA) was applied to calculate the band structure[53–55], the cutoff energy for the wave function was set to 50 Ry. The primitive unit cell of GeTe was used during the calculation and a dense *k* mesh of 30 × 30 × 30 was adopted for the Brillouin zone integration. Both cell parameters and atomic positions were fully relaxed until the force on each atom is less than 0.001eV/Å. Spin-orbit coupling (SOC) was considered during the calculation.

3.3 Results and Discussion

3.3.1 Phase Identification

Figure 3.1 shows the PXRD patterns of GeTe + *x wt*.% ZnO (*x* = 0, 0.5, 1.0, 1.5) before and after the ZEM measurements. All the diffraction peaks can be assigned to the GeTe phase (*R*3*m* #160) and Ge precipitations (marked by black stars). Ge precipitates result from the Ge deficiencies in GeTe, and they have been observed by other researchers.[56,57] Before the ZEM measurement, ZnO peaks (marked by orange arrows)

could be clearly observed; however, after the ZEM measurement, ZnO peaks disappeared completely, while two new peaks at 26° and 42° associated with ZnTe were observed. Rietveld XRD refinement performed via the Rietica software[58] confirmed the ZnTe impurity. Disappearance of ZnO and the development of ZnTe suggest one of the following reactions:

$$\mathrm{GeTe} + \ x\mathrm{ZnO} \rightarrow (1-x)\mathrm{GeTe} + \ x\mathrm{ZnTe} + x\mathrm{Ge} + \frac{1}{2}x\mathrm{O_2} \qquad 1$$

$$\mathrm{GeTe} + \ x\mathrm{ZnO} \rightarrow \ \mathrm{GeTe_{1-x}O}_x + xZnTe \qquad 2$$

The first reaction would not change the lattice constants of GeTe but would increase the amount of Ge precipitates. The second reaction would decrease the lattice constants of GeTe (O^{2-} is smaller than Te^{2-}) but would not change the amount of Ge precipitates. The lattice parameters (Table 2S) for the samples before and after the ZEM measurements are within 1 or 2 standard deviations, and thus Reaction 1 is the most likely one. Still, Reaction 2 cannot be excluded as the amount of incorporated O (even for x = 1.5 wt. %, 3.7 at. %) is small, and thus lattice constants may not change to a detectable level.

According to the refinement results, all three ZnO-doped samples show an increased amount of Ge precipitates after the ZEM measurements, but the changes in the samples with x = 1.0 and 1.5 wt. % are within the uncertainty.

Additionally, from the structural perspective, the substitution of O for Te in GeTe is unlikely, as the coordination environment for the O^{2-} anions in GeTe would be a distorted octahedron of Ge^{2+} cations, and O^{2-} tends to be either doubly coordinated as in GeO_2[59]or tetrahedrally coordinated as in amorphous GeO.[60] One additional consideration in support of Reaction 1 is a decrease in the carrier concentration, which is discussed below.

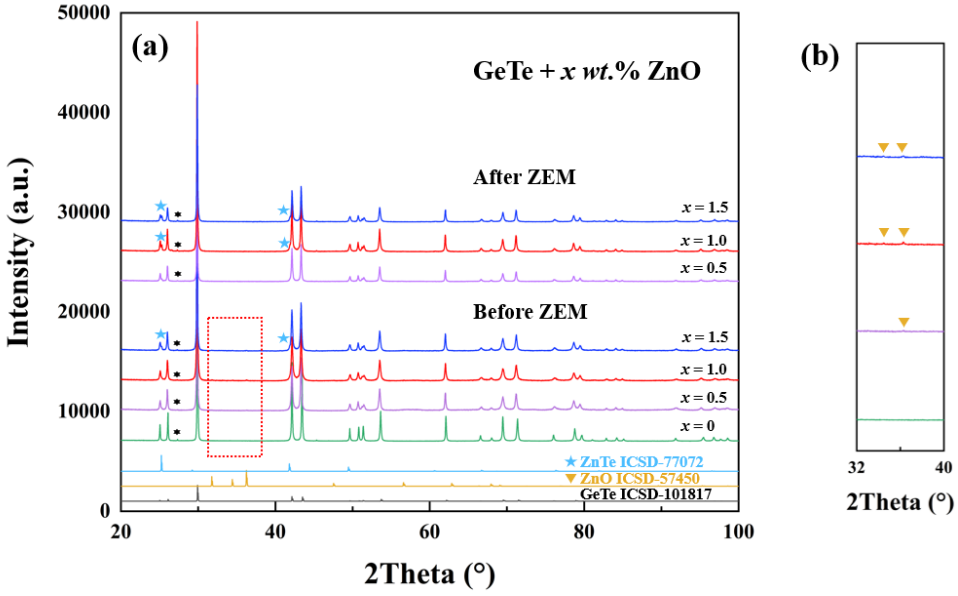

Figure 3.1. (a) XRD pattern of GeTe + *x wt*.% ZnO (*x* = 0, 0.5, 1.0, 1.5) before and after the ZEM measurement. The peaks marked by blue stars belongs to ZnTe, and those parked by black asterisks to Ge. (b) Zoom-in image of the area marked by red box; the orange arrows points to the ZnO peaks.

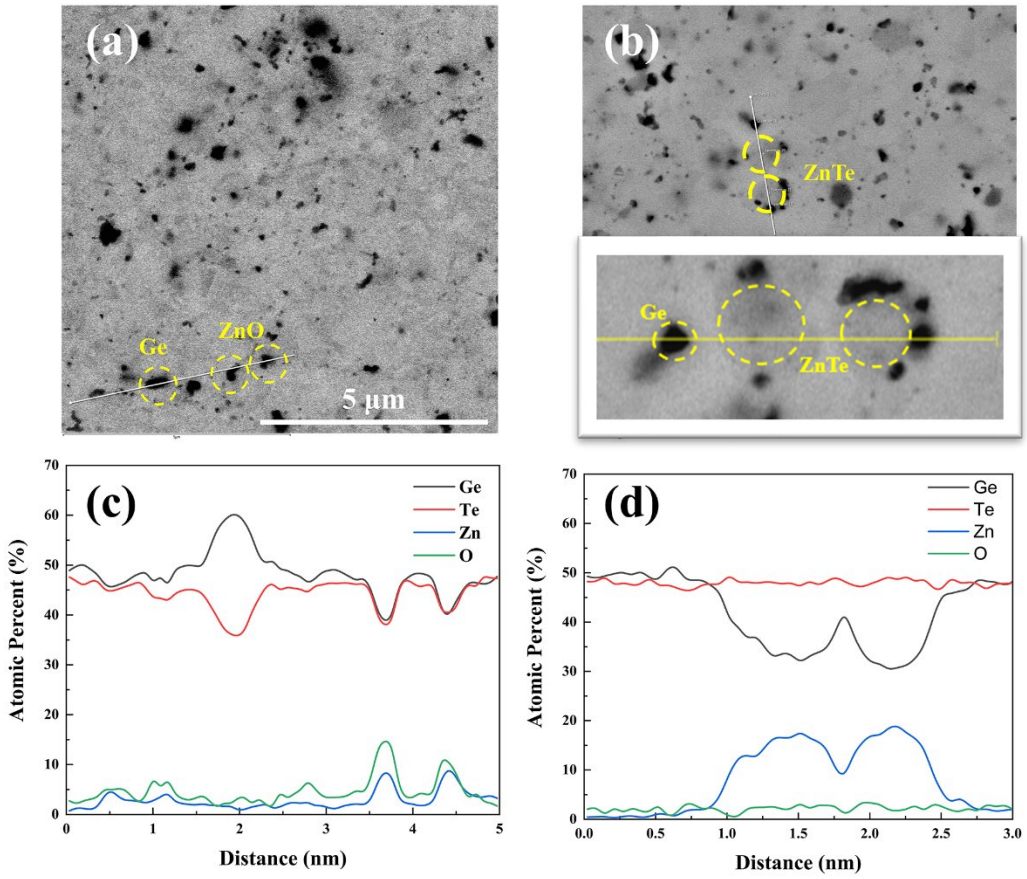

Figure 3.2. Backscattered electron (BSE) image of sample GeTe + 1.5 *wt. %* ZnO before ZEM (a) and after ZEM (b) with a zoomed-in line-scan XRD. (c) and (d) are the corresponding line scanning which clearly shows the formation of ZnTe after ZEM measurement.

The formation of ZnTe and disappearance of ZnO were confirmed via SEM analysis. **Figures 3. 2(a) and (b)** show the backscattered electron (BSE) images with elemental line scanning for the GeTe + 1.5 *wt*.% ZnO sample before and after the ZEM measurements, respectively. The EDS analysis shows that the dark spots in Figure 3.2(a) contain Zn and O elements and intrinsically present Ge precipitations. After the ZEM

measurement, the elemental analysis finds the dark spots being Ge precipitation surrounding the Zn- richer gray areas, indicating the formation of ZnTe and elemental Ge upon heating up the sample according to Reaction 1.

3.3.2 Thermoelectric Properties

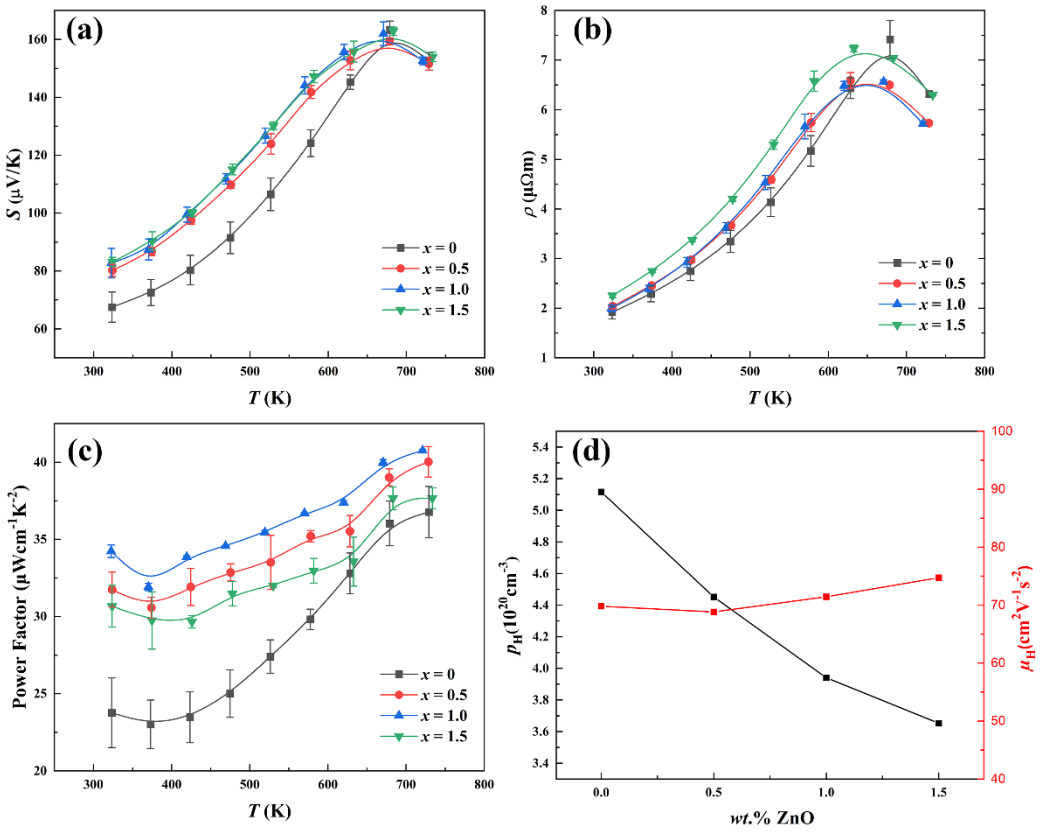

Figure 3.3 (a) Seebeck coefficient, (b) resistivity, (c) power factor (PF) and Hall measurement of GeTe + *x wt.*% ZnO (*x* = 0, 0.5, 1.0, 1.5)

Figure 3.3 shows the electrical properties of GeTe + *x wt.*% ZnO. The room temperature Seebeck coefficient is improved from 67μV/K in pristine GeTe to 83μV/K in

1.5 *wt*.% ZnO doped sample, which corresponds to the enhancement of 24%. Meanwhile, the electrical resistivity is slightly increased after the introduction of ZnO. As a result, the ZnO-doped samples, especially the one with 1.0 *wt*.% ZnO, exhibits enhanced power factors, PF (**Figure 3.3**(c)). To understand the origin of the enhanced Seebeck coefficient, Hall effect measurements were performed on all samples, and the results are shown in **Figure 3.3**(d). As can be seen, ZnO doping suppresses the carrier concentration of GeTe systematically, while the carrier mobility shows no significant changes. Detailed Hall data could be found in **Table S3.2 ~ 3.4** in the **Supplementary Materials**.

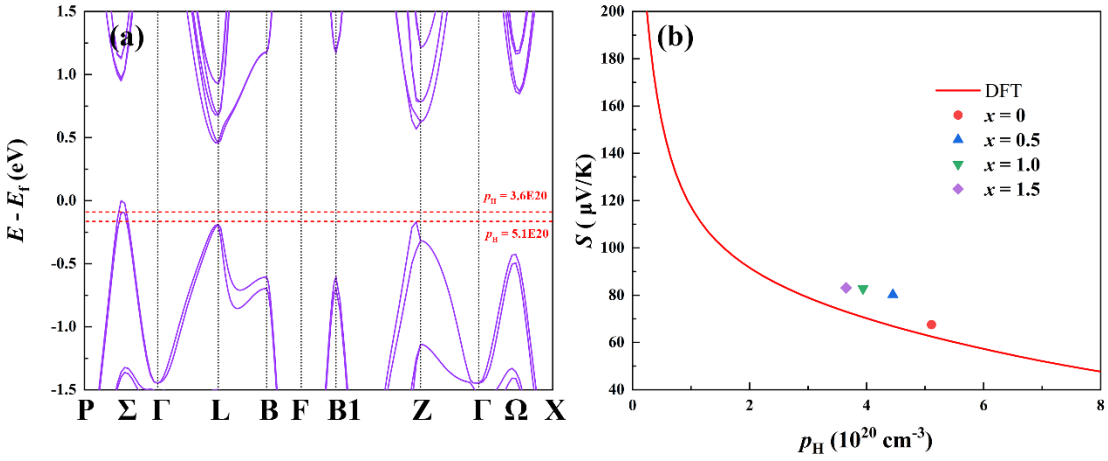

Figure 3.4 (a) Band structure of GeTe. (b) Room-temperature Pisarenko plot calculated via BoltzTraP[61]. Data points are determined by Hall measurement.

DFT calculations were performed to study the electrical properties of the materials. Based on the calculated band structure, the energy separation between the Σ and L bands $\Delta E_{\Sigma-\mathrm{L}}$ is 0.19eV, which is consistent with previous reports[5,62,63]. The two red dash lines represent the Fermi level before (carrier concentration 5.1×10^{20} cm^{-3}) and after (3.6×10^{20} cm^{-3}) doping with ZnO. The position of the Fermi level is based on the measured carrier concentration. Upon ZnO doping, the reduced carrier concentration led to an upward shift of the Fermi level. The energy separation of the Fermi level from the L and Z bands increased from 0eV to 0.025eV and from 0.075eV to 0.10eV, respectively. The enlarged energy separation limits the contributions of the L and Z bands toward the transport properties. DOS effective mass was calculated based on the single Kane band model (SKB). It was found that ZnO doping shows a negligible effect on the value of DOS effective mass. Based on the above analysis, the improvement in the Seebeck coefficient is mainly attributed to the reduced carrier concentration (**Figure 3.4** (b)).

To understand the mechanism behind the reduced carrier concentration, we compared the carrier concentration before and after the ZEM measurement, and the results are listed in **Table S3.2** and **Figure S3.1**. Interestingly, the carrier concentration of pure GeTe increases after the ZEM measurements, which can be attributed to increased Ge deficiencies after heating. In our HT diffraction studies on Bi-doped GeTe (unpublished

data), we have observed that heating above the rhombohedral-to-cubic transition leads to extra Ge precipitates, and this process is irreversible during cooling:

$$\mathrm{GeTe} \rightarrow \mathrm{Ge}_{1-x}\mathrm{Te} + x\mathrm{Ge} \quad (3)$$

The same can be assumed for GeTe, and this would explain an increase in the carrier concentration. On the other hand, all samples with ZnO show suppression of carrier concentration after heating. This could be explained by the formation of additional Ge precipitates (Reaction 1) above the level expected upon the rhombohedral-to-cubic transition. The surplus of Ge pushes some Ge back into the structure and compensates for the Ge vacancies that originated in the pristine GeTe. Such self-compensation was observed in other GeTe-based samples[42,64,65].

To further verify the role of Ge precipitates, we prepared the GeTe + GeO_2 sample with the oxygen content equivalent to that of the GeTe + 1 *wt*.% ZnO sample. The GeTe + GeO_2 sample shows the largest carrier concentration among all samples (**Table S2**). This can be rationalized by the fact that Ge precipitates are scavenged by GeO_2 to form amorphous GeO according to:

$$\mathrm{GeTe} + x\mathrm{GeO}_2 \rightarrow \mathrm{Ge}_{1-x}\mathrm{Te} + 2x\mathrm{GeO} \quad (4)$$

As a result, the formation of the Ge vacancies is promoted, and the carrier concentration is increased.

Electrical thermal conductivity was then calculated via Wiedemann-Franz law, $\kappa_e = L\sigma T$ .Lorenz numbers were calculated via the single Kane band model (SKB), which is presented in the **Supplementary Materials**. The lattice thermal conductivity, k_l, was obtained by subtracting the electrical thermal conductivity from the total thermal conductivity. The results are shown in **Figure 3.5**. It is worth noting that the total thermal conductivity of the pristine GeTe obtained from our experiment is generally lower than what has been reported in the literature[36,37,43,66]. The typical room-temperature thermal conductivity for GeTe ranges from 7.5 $Wm^{-1}K^{-1}$ to 8.5 $Wm^{-1}K^{-1,}$ while the value measured in our sample is 4.5 $Wm^{-1}K^{-1}$. This is attributed to the prolonged ball milling, which makes the grain size smaller than those in the literature.

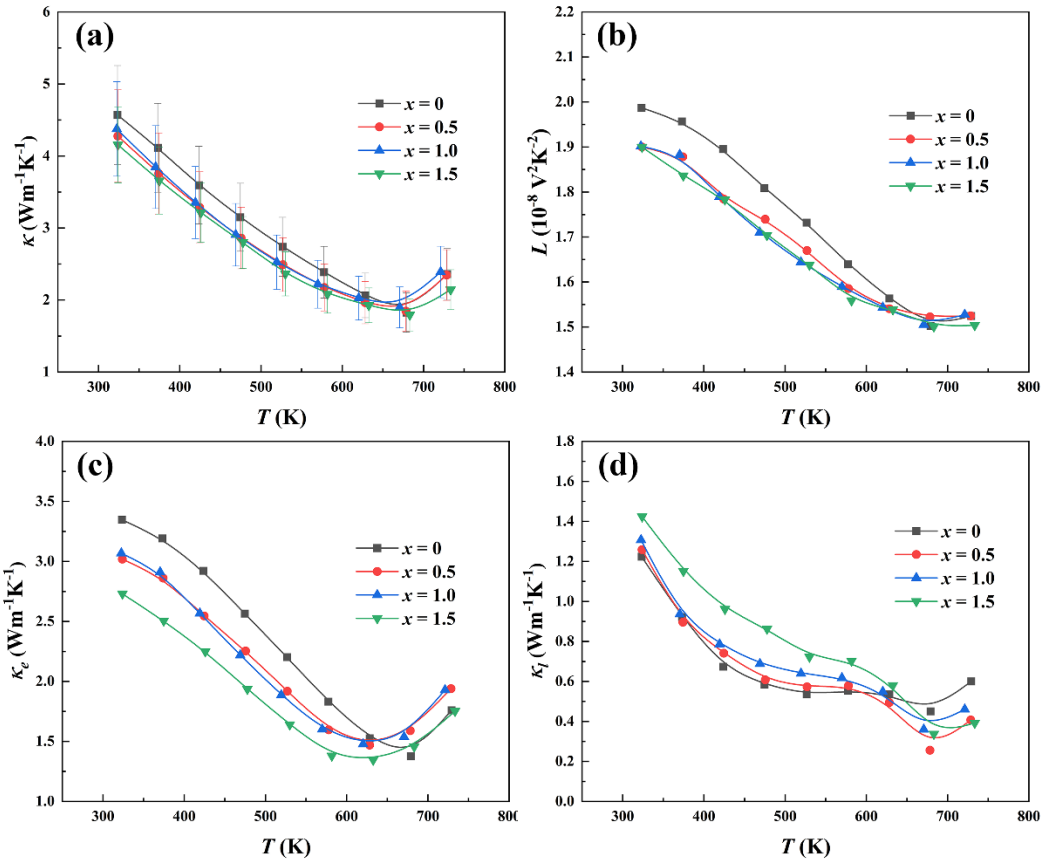

Figure 3.5 (a) Total thermal conductivity, (b) calculated Lorenz number, (c) electrical thermal conductivity and (d) lattice thermal conductivity. The lattice thermal conductivity were obtained by extracting the electrical thermal conductivity from the total thermal conductivity.

In all samples, the addition of ZnO suppresses the room-temperature electrical thermal conductivity, which can be attributed to the lower carrier concentration and extra carrier scattering introduced by the ZnTe nano inclusions. This reduction becomes less significant with temperature, indicating that acoustic phonon–electron scattering becomes dominant. Meanwhile, ZnO doping shows neglectable changes in lattice thermal

conductivity, and even increases the lattice conductivity slightly in the sample with 1.5 *wt.*% ZnO.

Using the above data, the figure of merit *zT* values are calculated and shown in **Figure 3.6**. Although ZnO doping has a negligible effect on the peak *zT* of GeTe, the average *zT* increased from 0.64 to 0.79, which corresponds to a 23% improvement.

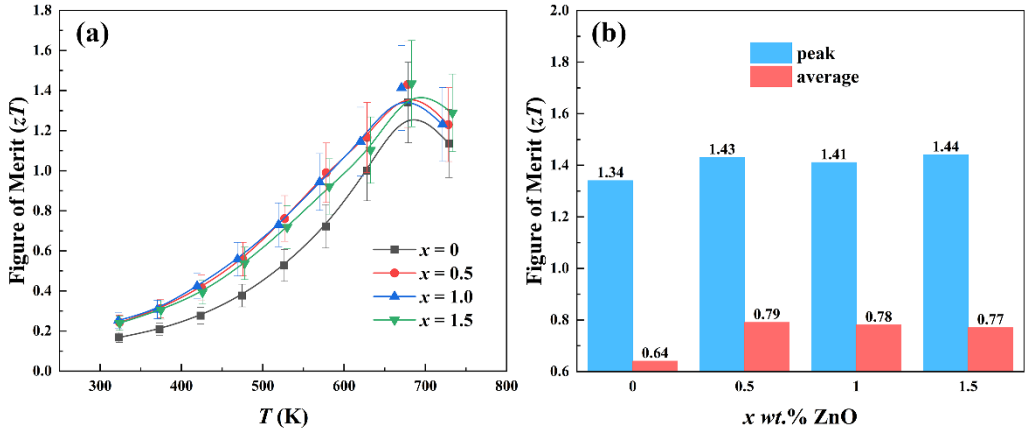

Figure 3.6 (a) *zT* values of GeTe + *x wt.*% ZnO (*x* = 0, 0.5, 1.0, 1.5). (b) Peak and average *zT* of GeTe + *x wt.*% ZnO (*x* = 0, 0.5, 1.0, 1.5).

3.4 Conclusion

In this work, we have demonstrated that the average power factor of GeTe could be improved by introducing a small amount of nanosized ZnO. At higher temperatures, ZnO particles react with the GeTe matrix and form the ZnTe particles. This reaction also yields

additional Ge, which leads to Ge self-compensation and lowers Ge deficiencies. Hall measurements show that the addition of ZnO decreased the carrier concentration from 5.1×10^{20} cm^{-3} to 3.6×10^{20} cm^{-3} and therefore supports the self-compensation mechanism. Due to the reduced carrier concentration and increased thermopower, an average zT value is increased by 23% to 0.79 in the 323-733K range.

References

1. Arachchige, I. U.; Kanatzidis, M. G. Anomalous Band Gap Evolution from Band Inversion in $Pb_{1-x}Sn_xTe$ Nanocrystals. *Nano Lett.* **2009**, *9* (4), 1583–1587. https://doi.org/10.1021/nl8037757.
2. Back, S. Y.; Yun, J. H.; Cho, H.; Byeon, S.; Jin, H.; Rhyee, J.-S. High Thermoelectric Performance by Chemical Potential Tuning and Lattice Anharmonicity in $GeTe_{1-x}I_x$ Compounds. *Inorg. Chem. Front.* **2021**, *8* (5), 1205–1214. https://doi.org/10.1039/D0QI01281E.
3. Banik, A.; Shenoy, U. S.; Anand, S.; Waghmare, U. V.; Biswas, K. Mg Alloying in SnTe Facilitates Valence Band Convergence and Optimizes Thermoelectric Properties. *Chem. Mater.* **2015**, *27* (2), 581–587. https://doi.org/10.1021/cm504112m.
4. Bu, Z.; Zhang, X.; Shan, B.; Tang, J.; Liu, H.; Chen, Z.; Lin, S.; Li, W.; Pei, Y. Realizing a 14% Single-Leg Thermoelectric Efficiency in GeTe Alloys. *Sci. Adv.* **2021**, *7* (19), eabf2738. https://doi.org/10.1126/sciadv.abf2738.
5. Li, J.; Zhang, X.; Chen, Z.; Lin, S.; Li, W.; Shen, J.; Witting, I. T.; Faghaninia, A.; Chen, Y.; Jain, A.; Chen, L.; Snyder, G. J.; Pei, Y. Low-Symmetry Rhombohedral GeTe Thermoelectrics. *Joule* **2018**, *2* (5), 976–987. https://doi.org/10.1016/j.joule.2018.02.016.
6. Bayikadi, K. S.; Wu, C. T.; Chen, L.-C.; Chen, K.-H.; Chou, F.-C.; Sankar, R. Synergistic Optimization of Thermoelectric Performance of Sb Doped GeTe with a Strained Domain and Domain Boundaries. *J. Mater. Chem. A* **2020**, *8* (10), 5332–5341. https://doi.org/10.1039/D0TA00628A.
7. Hong, M.; Wang, Y.; Liu, W.; Matsumura, S.; Wang, H.; Zou, J.; Chen, Z.-G. Arrays of Planar Vacancies in Superior Thermoelectric $Ge_{1-x-y}Cd_xBi_yTe$ with Band Convergence. *Adv. Energy Mater.* **2018**, *8* (30), 1801837. https://doi.org/10.1002/aenm.201801837.
8. Kuo, J. J.; Kang, S. D.; Imasato, K.; Tamaki, H.; Ohno, S.; Kanno, T.; Snyder, G. J. Grain Boundary Dominated Charge Transport in Mg_3Sb_2 -Based Compounds. *Energy Environ. Sci.* **2018**, *11* (2), 429–434. https://doi.org/10.1039/C7EE03326E.
9. Ma, J.; Delaire, O.; May, A. F.; Carlton, C. E.; McGuire, M. A.; VanBebber, L. H.; Abernathy, D. L.; Ehlers, G.; Hong, T.; Huq, A.; Tian, W.; Keppens, V. M.; Shao-Horn, Y.; Sales, B. C. Glass-like Phonon Scattering from a Spontaneous Nanostructure in AgSbTe2. *Nature Nanotech* **2013**, *8* (6), 445–451. https://doi.org/10.1038/nnano.2013.95.
10. Zhuang, H.; Pei, J.; Cai, B.; Dong, J.; Hu, H.; Sun, F.; Pan, Y.; Snyder, G. J.; Li, J. Thermoelectric Performance Enhancement in BiSbTe Alloy by Microstructure Modulation via Cyclic Spark Plasma Sintering with Liquid Phase. *Adv. Funct. Mater.* **2021**, *31* (15), 2009681. https://doi.org/10.1002/adfm.202009681.
11. Chen, R.; Qiu, P.; Jiang, B.; Hu, P.; Zhang, Y.; Yang, J.; Ren, D.; Shi, X.; Chen, L. Significantly Optimized Thermoelectric Properties in High-Symmetry Cubic Cu_7PSe_6 Compounds *via* Entropy Engineering. *J. Mater. Chem. A* **2018**, *6* (15), 6493–6502. https://doi.org/10.1039/C8TA00631H.
12. Fan, Z.; Wang, H.; Wu, Y.; Liu, X. J.; Lu, Z. P. Thermoelectric High-Entropy Alloys with Low Lattice Thermal Conductivity. *RSC Adv.* **2016**, *6* (57), 52164–52170. https://doi.org/10.1039/C5RA28088E.

13. Fan, Z.; Wang, H.; Wu, Y.; Liu, X.; Lu, Z. Thermoelectric Performance of PbSnTeSe High-Entropy Alloys. *Materials Research Letters* **2017**, *5* (3), 187–194. https://doi.org/10.1080/21663831.2016.1244116.
14. Hu, L.; Zhang, Y.; Wu, H.; Li, J.; Li, Y.; Mckenna, M.; He, J.; Liu, F.; Pennycook, S. J.; Zeng, X. Entropy Engineering of SnTe: Multi-Principal-Element Alloying Leading to Ultralow Lattice Thermal Conductivity and State-of-the-Art Thermoelectric Performance. *Adv. Energy Mater.* **2018**, *8* (29), 1802116. https://doi.org/10.1002/aenm.201802116.
15. Jiang, B.; Yu, Y.; Cui, J.; Liu, X.; Xie, L.; Liao, J.; Zhang, Q.; Huang, Y.; Ning, S.; Jia, B.; Zhu, B.; Bai, S.; Chen, L.; Pennycook, S. J.; He, J. High-Entropy-Stabilized Chalcogenides with High Thermoelectric Performance. *Science* **2021**, *371* (6531), 830–834. https://doi.org/10.1126/science.abe1292.
16. Qiu, Y.; Jin, Y.; Wang, D.; Guan, M.; He, W.; Peng, S.; Liu, R.; Gao, X.; Zhao, L.-D. Realizing High Thermoelectric Performance in GeTe through Decreasing the Phase Transition Temperature *via* Entropy Engineering. *J. Mater. Chem. A* **2019**, *7* (46), 26393–26401. https://doi.org/10.1039/C9TA10963C.
17. Shafeie, S.; Guo, S.; Hu, Q.; Fahlquist, H.; Erhart, P.; Palmqvist, A. High-Entropy Alloys as High-Temperature Thermoelectric Materials. *Journal of Applied Physics* **2015**, *118* (18), 184905. https://doi.org/10.1063/1.4935489.
18. Yan, J.; Liu, F.; Ma, G.; Gong, B.; Zhu, J.; Wang, X.; Ao, W.; Zhang, C.; Li, Y.; Li, J. Suppression of the Lattice Thermal Conductivity in NbFeSb-Based Half-Heusler Thermoelectric Materials through High Entropy Effects. *Scripta Materialia* **2018**, *157*, 129–134. https://doi.org/10.1016/j.scriptamat.2018.08.008.
19. Delaire, O.; Ma, J.; Marty, K.; May, A. F.; McGuire, M. A.; Du, M.-H.; Singh, D. J.; Podlesnyak, A.; Ehlers, G.; Lumsden, M.; Sales, B. C. Giant Anharmonic Phonon Scattering in PbTe. *Nature Mater* **2011**, *10* (8), 614–619. https://doi.org/10.1038/nmat3035.
20. Liu, H.; Chen, Z.; Tang, J.; Zhong, Y.; Guo, X.; Zhang, F.; Ang, R. High Quality Factor Enabled by Multiscale Phonon Scattering for Enhancing Thermoelectrics in Low-Solubility n-Type PbTe–Cu $_2$ Te Alloys. *ACS Appl. Mater. Interfaces* **2020**, *12* (47), 52952–52958. https://doi.org/10.1021/acsami.0c16431.
21. Pei, Y.; LaLonde, A.; Iwanaga, S.; Snyder, G. J. High Thermoelectric Figure of Merit in Heavy Hole Dominated PbTe. *Energy Environ. Sci.* **2011**, *4* (6), 2085. https://doi.org/10.1039/c0ee00456a.
22. Pei, Y.; May, A. F.; Snyder, G. J. Self-Tuning the Carrier Concentration of PbTe/Ag2Te Composites with Excess Ag for High Thermoelectric Performance. *Adv. Energy Mater.* **2011**, *1* (2), 291–296. https://doi.org/10.1002/aenm.201000072.
23. Wu, H. J.; Zhao, L.-D.; Zheng, F. S.; Wu, D.; Pei, Y. L.; Tong, X.; Kanatzidis, M. G.; He, J. Q. Broad Temperature Plateau for Thermoelectric Figure of Merit ZT>2 in Phase-Separated PbTe0.7S0.3. *Nat Commun* **2014**, *5* (1), 4515. https://doi.org/10.1038/ncomms5515.
24. Rawat, P. K.; Paul, B.; Banerji, P. Exploration of Zn Resonance Levels and Thermoelectric Properties in I-Doped PbTe with ZnTe Nanostructures. *ACS Appl. Mater. Interfaces* **2014**, *6* (6), 3995–4004. https://doi.org/10.1021/am405410e.

25. Wang, S.; Xiao, Y.; Chen, Y.; Peng, S.; Wang, D.; Hong, T.; Yang, Z.; Sun, Y.; Gao, X.; Zhao, L.-D. Hierarchical Structures Lead to High Thermoelectric Performance in Cu $_{m+n}$ Pb $_{100}$ Sb $_{m}$ Te $_{100}$ Se $_{2m}$ (CLAST). *Energy Environ. Sci.* **2021**, *14* (1), 451–461. https://doi.org/10.1039/D0EE03459B.
26. Asfandiyar; Cai, B.; Zhuang, H.-L.; Tang, H.; Li, J.-F. Polycrystalline SnSe–Sn1–vS Solid Solutions: Vacancy Engineering and Nanostructuring Leading to High Thermoelectric Performance. *Nano Energy* **2020**, *69*, 104393. https://doi.org/10.1016/j.nanoen.2019.104393.
27. Chen, Z.-G.; Shi, X.; Zhao, L.-D.; Zou, J. High-Performance SnSe Thermoelectric Materials: Progress and Future Challenge. *Progress in Materials Science* **2018**, *97*, 283–346. https://doi.org/10.1016/j.pmatsci.2018.04.005.
28. Duong, A. T.; Nguyen, V. Q.; Duvjir, G.; Duong, V. T.; Kwon, S.; Song, J. Y.; Lee, J. K.; Lee, J. E.; Park, S.; Min, T.; Lee, J.; Kim, J.; Cho, S. Achieving ZT=2.2 with Bi-Doped n-Type SnSe Single Crystals. *Nat Commun* **2016**, *7* (1), 13713. https://doi.org/10.1038/ncomms13713.
29. Li, S.; Lou, X.; Li, X.; Zhang, J.; Li, D.; Deng, H.; Liu, J.; Tang, G. Realization of High Thermoelectric Performance in Polycrystalline Tin Selenide through Schottky Vacancies and Endotaxial Nanostructuring. *Chem. Mater.* **2020**, *32* (22), 9761–9770. https://doi.org/10.1021/acs.chemmater.0c03657.
30. Li, Y.; He, B.; Heremans, J. P.; Zhao, J.-C. High-Temperature Oxidation Behavior of Thermoelectric SnSe. *Journal of Alloys and Compounds* **2016**, *669*, 224–231. https://doi.org/10.1016/j.jallcom.2016.01.258.
31. Li, Y.; Li, F.; Dong, J.; Ge, Z.; Kang, F.; He, J.; Du, H.; Li, B.; Li, J.-F. Enhanced Mid-Temperature Thermoelectric Performance of Textured SnSe Polycrystals Made of Solvothermally Synthesized Powders. *J. Mater. Chem. C* **2016**, *4* (10), 2047–2055. https://doi.org/10.1039/C5TC04202J.
32. Qin, B.; Zhang, Y.; Wang, D.; Zhao, Q.; Gu, B.; Wu, H.; Zhang, H.; Ye, B.; Pennycook, S. J.; Zhao, L.-D. Ultrahigh Average *ZT* Realized in p-Type SnSe Crystalline Thermoelectrics through Producing Extrinsic Vacancies. *J. Am. Chem. Soc.* **2020**, *142* (12), 5901–5909. https://doi.org/10.1021/jacs.0c01726.
33. Wu, T.; Chen, X.; Xie, H.; Chen, Z.; Zhang, L.; Pan, Z.; Zhuang, W. Coupling of Spin-Orbit Interaction with Phonon Anharmonicity Leads to Significant Impact on Thermoelectricity in SnSe. *Nano Energy* **2019**, *60*, 673–679. https://doi.org/10.1016/j.nanoen.2019.04.010.
34. Zhao, L.-D.; Tan, G.; Hao, S.; He, J.; Pei, Y.; Chi, H.; Wang, H.; Gong, S.; Xu, H.; Dravid, V. P.; Uher, C.; Snyder, G. J.; Wolverton, C.; Kanatzidis, M. G. Ultrahigh Power Factor and Thermoelectric Performance in Hole-Doped Single-Crystal SnSe. *Science* **2016**, *351* (6269), 141–144. https://doi.org/10.1126/science.aad3749.
35. Zhou, C.; Lee, Y. K.; Yu, Y.; Byun, S.; Luo, Z.-Z.; Lee, H.; Ge, B.; Lee, Y.-L.; Chen, X.; Lee, J. Y.; Cojocaru-Mirédin, O.; Chang, H.; Im, J.; Cho, S.-P.; Wuttig, M.; Dravid, V. P.; Kanatzidis, M. G.; Chung, I. Polycrystalline SnSe with a Thermoelectric Figure of Merit Greater than the Single Crystal. *Nat. Mater.* **2021**, *20* (10), 1378–1384. https://doi.org/10.1038/s41563-021-01064-6.

36. Acharyya, P.; Roychowdhury, S.; Samanta, M.; Biswas, K. Ultralow Thermal Conductivity, Enhanced Mechanical Stability, and High Thermoelectric Performance in $(GeTe)_{1-2x}(SnSe)_x(SnS)_x$. *J. Am. Chem. Soc.* **2020**, *142* (48), 20502–20508. https://doi.org/10.1021/jacs.0c11015.
37. Bayikadi, K. S.; Sankar, R.; Wu, C. T.; Xia, C.; Chen, Y.; Chen, L.-C.; Chen, K.-H.; Chou, F.-C. Enhanced Thermoelectric Performance of GeTe through *in Situ* Microdomain and Ge-Vacancy Control. *J. Mater. Chem. A* **2019**, *7* (25), 15181–15189. https://doi.org/10.1039/C9TA03503F.
38. Bhat, D. K.; Shenoy, U. S. Resonance Levels in GeTe Thermoelectrics: Zinc as a New Multifaceted Dopant. *New J. Chem.* **2020**, *44* (41), 17664–17670. https://doi.org/10.1039/D0NJ04273K.
39. Bu, Z.; Li, W.; Li, J.; Zhang, X.; Mao, J.; Chen, Y.; Pei, Y. Dilute Cu2Te-Alloying Enables Extraordinary Performance of r-GeTe Thermoelectrics. *Materials Today Physics* **2019**, *9*, 100096. https://doi.org/10.1016/j.mtphys.2019.100096.
40. Cao, J.; Chien, S. W.; Tan, X. Y.; Tan, C. K. I.; Zhu, Q.; Wu, J.; Wang, X.; Zhao, Y.; Yang, L.; Yan, Q.; Liu, H.; Xu, J.; Suwardi, A. Realizing ZT Values of 2.0 in Cubic GeTe. *ChemNanoMat* **2021**, *7* (4), 476–482. https://doi.org/10.1002/cnma.202100033.
41. Chen, S.; Bai, H.; Li, J.; Pan, W.; Jiang, X.; Li, Z.; Chen, Z.; Yan, Y.; Su, X.; Wu, J.; Uher, C.; Tang, X. Vacancy-Based Defect Regulation for High Thermoelectric Performance in $Ge_9Sb_2Te_{12-x}$ Compounds. *ACS Appl. Mater. Interfaces* **2020**, *12* (17), 19664–19673. https://doi.org/10.1021/acsami.0c02155.
42. Dong, J.; Sun, F.-H.; Tang, H.; Pei, J.; Zhuang, H.-L.; Hu, H.-H.; Zhang, B.-P.; Pan, Y.; Li, J.-F. Medium-Temperature Thermoelectric GeTe: Vacancy Suppression and Band Structure Engineering Leading to High Performance. *Energy Environ. Sci.* **2019**, *12* (4), 1396–1403. https://doi.org/10.1039/C9EE00317G.
43. Dou, Y.; Li, J.; Xie, Y.; Wu, X.; Hu, L.; Liu, F.; Ao, W.; Liu, Y.; Zhang, C. Lone-Pair Engineering: Achieving Ultralow Lattice Thermal Conductivity and Enhanced Thermoelectric Performance in Al-Doped GeTe-Based Alloys. *Materials Today Physics* **2021**, *20*, 100497. https://doi.org/10.1016/j.mtphys.2021.100497.
44. Duan, S.; Xue, W.; Yao, H.; Wang, X.; Wang, C.; Li, S.; Zhang, Z.; Yin, L.; Bao, X.; Huang, L.; Wang, X.; Chen, C.; Sui, J.; Chen, Y.; Mao, J.; Cao, F.; Wang, Y.; Zhang, Q. Achieving High Thermoelectric Performance by $NaSbTe_2$ Alloying in GeTe for Simultaneous Suppression of Ge Vacancies and Band Tailoring. *Advanced Energy Materials* **2022**, *12* (3), 2103385. https://doi.org/10.1002/aenm.202103385.
45. Fahrnbauer, F.; Souchay, D.; Wagner, G.; Oeckler, O. High Thermoelectric Figure of Merit Values of Germanium Antimony Tellurides with Kinetically Stable Cobalt Germanide Precipitates. *J. Am. Chem. Soc.* **2015**, *137* (39), 12633–12638. https://doi.org/10.1021/jacs.5b07856.
46. Hong, M.; Wang, Y.; Feng, T.; Sun, Q.; Xu, S.; Matsumura, S.; Pantelides, S. T.; Zou, J.; Chen, Z.-G. Strong Phonon–Phonon Interactions Securing Extraordinary Thermoelectric $Ge_{1-x}Sb_xTe$ with Zn-Alloying-Induced Band Alignment. *J. Am. Chem. Soc.* **2019**, *141* (4), 1742–1748. https://doi.org/10.1021/jacs.8b12624.
47. Li, M.; Hong, M.; Tang, X.; Sun, Q.; Lyu, W.-Y.; Xu, S.-D.; Kou, L.-Z.; Dargusch, M.; Zou, J.; Chen, Z.-G. Crystal Symmetry Induced Structure and Bonding Manipulation

Boosting Thermoelectric Performance of GeTe. *Nano Energy* **2020**, *73*, 104740. https://doi.org/10.1016/j.nanoen.2020.104740.
48. Zheng, Z.; Su, X.; Deng, R.; Stoumpos, C.; Xie, H.; Liu, W.; Yan, Y.; Hao, S.; Uher, C.; Wolverton, C.; Kanatzidis, M. G.; Tang, X. Rhombohedral to Cubic Conversion of GeTe via MnTe Alloying Leads to Ultralow Thermal Conductivity, Electronic Band Convergence, and High Thermoelectric Performance. *J. Am. Chem. Soc.* **2018**, *140* (7), 2673–2686. https://doi.org/10.1021/jacs.7b13611.
49. Li, J.; Chen, Z.; Zhang, X.; Sun, Y.; Yang, J.; Pei, Y. Electronic Origin of the High Thermoelectric Performance of GeTe among the P-Type Group IV Monotellurides. *NPG Asia Mater* **2017**, *9* (3), e353–e353. https://doi.org/10.1038/am.2017.8.
50. Wu, D.; Zhao, L.-D.; Hao, S.; Jiang, Q.; Zheng, F.; Doak, J. W.; Wu, H.; Chi, H.; Gelbstein, Y.; Uher, C.; Wolverton, C.; Kanatzidis, M.; He, J. Origin of the High Performance in GeTe-Based Thermoelectric Materials upon Bi_2Te_3 Doping. *J. Am. Chem. Soc.* **2014**, *136* (32), 11412–11419. https://doi.org/10.1021/ja504896a.
51. Giannozzi, P.; Baroni, S.; Bonini, N.; Calandra, M.; Car, R.; Cavazzoni, C.; Ceresoli, D.; Chiarotti, G. L.; Cococcioni, M.; Dabo, I.; Dal Corso, A.; de Gironcoli, S.; Fabris, S.; Fratesi, G.; Gebauer, R.; Gerstmann, U.; Gougoussis, C.; Kokalj, A.; Lazzeri, M.; Martin-Samos, L.; Marzari, N.; Mauri, F.; Mazzarello, R.; Paolini, S.; Pasquarello, A.; Paulatto, L.; Sbraccia, C.; Scandolo, S.; Sclauzero, G.; Seitsonen, A. P.; Smogunov, A.; Umari, P.; Wentzcovitch, R. M. QUANTUM ESPRESSO: A Modular and Open-Source Software Project for Quantum Simulations of Materials. *J. Phys.: Condens. Matter* **2009**, *21* (39), 395502. https://doi.org/10.1088/0953-8984/21/39/395502.
52. Giannozzi, P.; Baseggio, O.; Bonfà, P.; Brunato, D.; Car, R.; Carnimeo, I.; Cavazzoni, C.; de Gironcoli, S.; Delugas, P.; Ferrari Ruffino, F.; Ferretti, A.; Marzari, N.; Timrov, I.; Urru, A.; Baroni, S. Q UANTUM ESPRESSO toward the Exascale. *J. Chem. Phys.* **2020**, *152* (15), 154105. https://doi.org/10.1063/5.0005082.
53. Dal Corso, A. Pseudopotentials Periodic Table: From H to Pu. *Computational Materials Science* **2014**, *95*, 337–350. https://doi.org/10.1016/j.commatsci.2014.07.043.
54. Prandini, G.; Marrazzo, A.; Castelli, I. E.; Mounet, N.; Marzari, N. Precision and Efficiency in Solid-State Pseudopotential Calculations. *npj Comput Mater* **2018**, *4* (1), 72. https://doi.org/10.1038/s41524-018-0127-2.
55. Tran, F.; Blaha, P. Accurate Band Gaps of Semiconductors and Insulators with a Semilocal Exchange-Correlation Potential. *Phys. Rev. Lett.* **2009**, *102* (22), 226401. https://doi.org/10.1103/PhysRevLett.102.226401.
56. Li, J., Chen, Z., Zhang, X., Yu, H., Wu, Z., Xie, H., Chen, Y., and Pei, Y. (2017). Simultaneous optimization of carrier concentration and alloy scattering for ultrahigh performance GeTe thermoelectrics. *Adv. Sci*. 4, 1700341.
57. Zhang, X., Li, J., Wang, X., Chen, Z., Mao, J., Chen, Y., and Pei, Y. (2018). Vacancy manipulation for thermoelectric enhancements in GeTe alloys. *J. Am. Chem. Soc.* 140, 15883–15888.
58. Hunter, B. A. Rietica - a Visual Rietveld Program; Australia, 2000; p 24.
59. Smith, G. S.; Isaacs, P. B. The Crystal Structure of Quartz-like GEO2. *Acta Crystallographica* **1964, *17 (7), 842–846.***

60. Semiconductors, 2020, Vol. 54, No. 12, pp. 1555–1560. © Pleiades Publishing, Ltd., 2020
61. Madsen, G. K. H.; Singh, D. J. BoltzTraP. A Code for Calculating Band-Structure Dependent Quantities. *Computer Physics Communications* **2006**, *175* (1), 67–71. https://doi.org/10.1016/j.cpc.2006.03.007.
62. Hong, M.; Zou, J.; Chen, Z. Thermoelectric GeTe with Diverse Degrees of Freedom Having Secured Superhigh Performance. *Adv. Mater.* **2019**, *31* (14), 1807071. https://doi.org/10.1002/adma.201807071.
63. Hong, M.; Lyv, W.; Li, M.; Xu, S.; Sun, Q.; Zou, J.; Chen, Z.-G. Rashba Effect Maximizes Thermoelectric Performance of GeTe Derivatives. *Joule* **2020**, *4* (9), 2030–2043. https://doi.org/10.1016/j.joule.2020.07.021.
64. Jin, Y.; Xiao, Y.; Wang, D.; Huang, Z.; Qiu, Y.; Zhao, L.-D. Realizing High Thermoelectric Performance in GeTe through Optimizing Ge Vacancies and Manipulating Ge Precipitates. *ACS Appl. Energy Mater.* **2019**, *2* (10), 7594–7601. https://doi.org/10.1021/acsaem.9b01585.
65. Suwardi, A.; Cao, J.; Zhao, Y.; Wu, J.; Chien, S. W.; Tan, X. Y.; Hu, L.; Wang, X.; Wang, W.; Li, D.; Yin, Y.; Zhou, W.-X.; Repaka, D. V. M.; Chen, J.; Zheng, Y.; Yan, Q.; Zhang, G.; Xu, J. Achieving High Thermoelectric Quality Factor toward High Figure of Merit in GeTe. *Materials Today Physics* **2020**, *14*, 100239. https://doi.org/10.1016/j.mtphys.2020.100239.
66. Perumal, S.; Samanta, M.; Ghosh, T.; Shenoy, U. S.; Bohra, A. K.; Bhattacharya, S.; Singh, A.; Waghmare, U. V.; Biswas, K. Realization of High Thermoelectric Figure of Merit in GeTe by Complementary Co-Doping of Bi and In. *Joule* **2019**, *3* (10), 2565–2580. https://doi.org/10.1016/j.joule.2019.08.017.

Chapter 3 Supplementary Information

Single Kane Band Model

Since GeTe is a narrow band gap semiconductor, strong interactions between the conduction and valence bands make the non-parabolicity at the valence bands' maxima impossible to ignore. To consider this effect, a Single-Kane Band (SKB) model was developed to calculate the Lorenz number and DOS effective mass based on Pei et al.'s work[1]. The expressions for the transport coefficients are as follow:

Seebeck coefficient S

$$S = \frac{k_B}{e}\left[\frac{{}^1F_{-2}^1}{{}^0F_{-2}^1} - \xi\right] \tag{S3.1}$$

Lorenz number L

$$L = \left(\frac{k_B}{e}\right)^2\left[\frac{{}^2F_{-2}^1}{{}^0F_{-2}^1} - \left(\frac{{}^1F_{-2}^1}{{}^0F_{-2}^1}\right)^2\right] \tag{S3.2}$$

Single band effective mass m_b^*

$$m_b^* = \frac{1}{2k_BT}\left[\frac{3Ap_H\pi^2\hbar^3}{N_V}\left({}^0F_0^{3/2}\right)^{-1}\right]^{2/3} \tag{S3.3}$$

Hall factor A

$$A = \frac{3K(K+2)}{(2K+1)^2}\frac{{}^0F_{-4}^{1/2}\,{}^0F_0^{3/2}}{\left({}^0F_{-2}^1\right)^2} \tag{S3.4}$$

Where ${}^nF_k^m$ is the α included Fermi integral

$${}^nF_k^m = \int_0^\infty\left(-\frac{\partial f}{\partial\varepsilon}\right)\varepsilon^n(\varepsilon+\alpha\varepsilon^2)^m[(1+2\alpha\varepsilon)^2+2]^{k/2}d\varepsilon \tag{S3.5}$$

ε ($\varepsilon = E / k_BT$)is the reduced energy, f is the Fermi-Dirac distribution, α ($\alpha = k_BT / E_g$) is the non-parabolic parameter, E_g is the band gap (0.63eV for GeTe), ξ ($\xi = E_f / k_BT$) is the

reduced Fermi level, N_v is the band degeneracy, $K = m_{//}^* / m_{\perp}^*$ is the anisotropy factor. For GeTe, $K = 2^2$.

Table S3.1. Cell parameters and density of GeTe + *x wt*.% ZnO (*x* = 0, 0.5, 1.0, 1.5).

Composition	*a* parameter (Å)	*c* parameter (Å)	Impurities	Density (g/cm^3)	Relative Density (%)
	Before ZEM				
x = 0	4.174(1)	10.643(4)	N/A	5.97	96.6
x = 0.5	4.174(1)	10.643(4)	ZnTe-1.1(8)% Ge-0.3(1)%	5.98	96.8
x = 1.0	4.174(1)	10.642(4)	ZnO-0.3(5)% ZnTe-1.1(8)% Ge-0.3(1)%	5.88	95.2
x = 1.5	4.174(1)	10.645(4)	ZnO-0.3(5)% ZnTe-2.2(1)% Ge-0.5(1)%	5.88	95.2
	After ZEM				
x = 0	4.174(1)	10.643(4)	N/A	5.97	96.6
x = 0.5	4.175(1)	10.649(3)	ZnTe-1.7(9)% Ge-0.7(1)%	5.98	96.8
x = 1.0	4.176(1)	10.649(3)	ZnTe-3.0(9)% Ge-0.3(0)%	5.88	95.2
x = 1.5	4.176(1)	10.647(4)	ZnTe-4.1(1)% Ge-0.6(1)%	5.88	95.2

Table S3.2. Hall data of GeTe + *x wt*.% ZnO (*x* = 0, 0.5, 1.0, 1.5) before and after ZEM.

Composition	**Carrier Concentration (10^{20} cm^{-3})**	**Mobility (cm^{2}V^{-1}s^{-2})**	**DOS Effective Mass (m_e)**
Before ZEM			
x = 0	3.9	79.5	N/A
x = 0.5	5.4	60.6	N/A
x = 1.0	6.6	52.7	N/A
x = 1.5	5.4	65.9	N/A
After ZEM			
x = 0	5.1	69.8	2.0
x = 0.5	4.4	68.8	2.1
x = 1.0	3.9	71.4	2.0
x = 1.5	3.6	74.7	1.9
GeO_2	12.4	28.8	N/A

Because of the thermal instability during the ZEM measurements, the DOS effective mass could not be determined for the samples labeled "before ZEM".

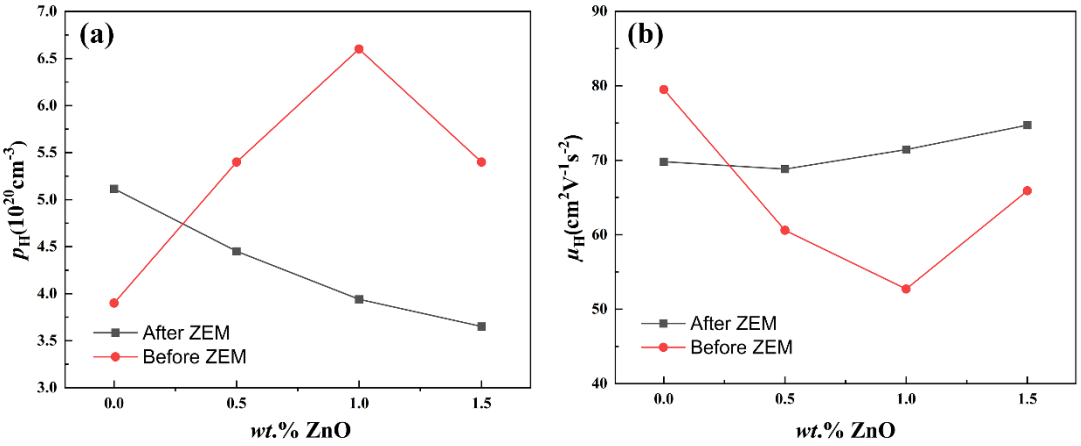

Figure S3.1. (a) Carrier concentration and (b) Hall mobility before and after the ZEM.

References

1. Pei, Y.; LaLonde, A. D.; Wang, H.; Snyder, G. J. Low Effective Mass Leading to High Thermoelectric Performance. *Energy Environ. Sci.* **2012**, *5* (7), 7963. https://doi.org/10.1039/c2ee21536e.
2. Madelung, O.; Rössler, U.; Schulz, M. *General Introduction: Datasheet from Landolt-Börnstein - Group III Condensed Matter · Volume 41C: "Non-Tetrahedrally Bonded Elements and Binary Compounds I" in SpringerMaterials (Https://Doi.Org/10.1007/10681727_1)*; Springer-Verlag Berlin Heidelberg. https://doi.org/10.1007/10681727_1.

Chapter 4. Converting n-Type $Co_4Ge_6Te_6$ Skuttertudite into p-Type and Enhancing its Thermoelectric Properties through Fe Substitution

The content discussed in this chapter is based on the manuscript of "Converting n-Type $Co_4Ge_6Te_6$ Skutterudite into *p*-Type and Enhancing its Thermoelectric Properties through Fe Substitution", which was published in the Journal of Alloys and Compounds, 2022 Vol. 913, p.165314. Shaochang Song and Yuyang Huang carried out the experimental procedures, data analysis, and visualization of the properties. Dr. Yu-Chih Tseng, Ph.D. candidate Suneesh Meledath Valiyaveettil and Dr. Kuei-Hsien Chen helped with the physical property measurements.

4.1. Introduction

In recent years, environmental issues prompted a growing interest in thermoelectric materials due to their ability to directly convert waste heat into electricity without any adverse environmental impacts.[1] Usually, the efficiency of thermoelectric material is determined by the dimensionless figure of merit, zT:$zT = \frac{\alpha^2\sigma}{\kappa C+\kappa l}T$, where α, σ, κ_C, κ_l and T are Seebeck coefficient, electrical conductivity, carrier thermal conductivity, lattice conductivity, and absolute temperature, respectively.[2] Most ideally, thermoelectric material is expected to behave as a phonon-glass electron-crystal (PGEC), which has a high, crystal-like electrical conductivity and a low, glass-like thermal conductivity.[3] However,

since α, σ are interconnected via the charge carrier concentration and inversely proportional to each other, and only κl could be modified independently[3], it is challenging to maximize each parameter and find a simple material to work as a PGEC. Modern engineering strategies maximize the thermoelectric efficiency to the fullest extent, including band structure sculpture to enhance the power factor[4-8], carrier concentration optimization[9-12], and introduction of nano-construction to suppress lattice thermal conductivity.[16-18]

Binary skutterudites have the general formula MX_3 and adopt the space group $Im\bar{3}$ (M = Co, Rh or Ir; X = P, As, or Sb). The MX_3 structures contain X_4 rectangular anion rings formed by tilted MX_6 octahedra.[19-21] The binary $CoSb_3$ skutterudite attracted extensive interest as it possesses excellent charge transport properties.[22,23] However, it also displays high thermal conductivity, limiting its thermoelectric performance. Electropositive atoms can fill Large voids present in the MX_3 systems increasing electrical conductivity and significantly suppressing lattice thermal conductivity synergistically[24-28]; a general formula AyM_4X_{12} can represent the composition of these filled skutterudites.[29]

To further reduce lattice thermal conductivity, an isoelectric substitution on the anion site in the binary system by two aliovalent p elements leads to a ternary anion-mixed skutterudites $AX_{1.5}Y_{1.5}$. $CoGe_{1.5}Y_{1.5}$ (Y = S, Se) is one member of such a group[30], and its

structure was refined by Vaqueiro et al. using powder neutron diffraction.[31] Figure 4.1 shows the crystal structures of $CoSb_3$ and $CoGe_{1.5}Te_{1.5}$. In the binary $CoSb_3$ structure, the four-membered Sb ring forms into a rectangle.[32] However, in the $CoGe_{1.5}Te_{1.5,}$ the $[Ge_2Te_2]^{-4}$ rings exist two crystallographic angles shown in Figure 4.1(c).[31] Moreover, the anion rings are arranged perpendicular to the [111] direction in the unit cell more like a diamond shape rather than a rectendular.[31] A symmetry reduction is expected from $Im\bar{3}$ to $R\bar{3}$.[31] Interestingly, $CoGe_{1.5}Te_{1.5}$ undergoes a phase transition from rohbomhedral to cubic at 610°C.[33]

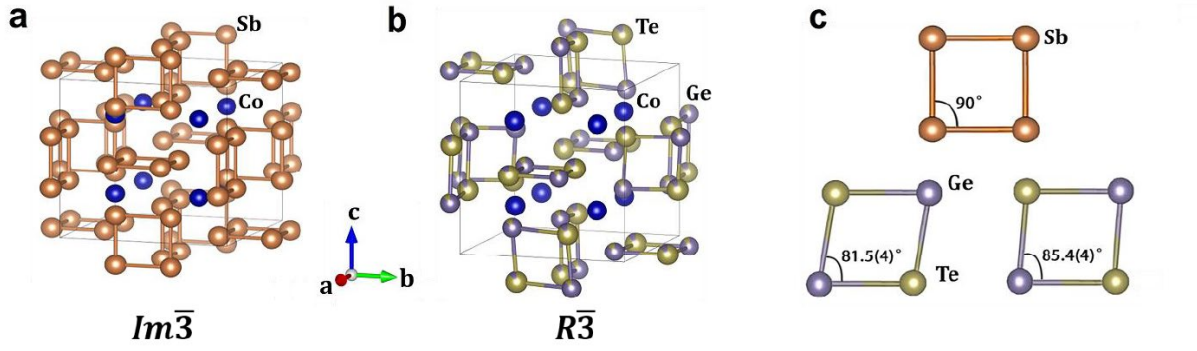

Figure 4.1. Crystal structure of (a) $CoSb_3$32 (space group $Im\bar{3}$) and (b) $CoGe_{1.5}Te_{1.5}$[34] (space group $R\bar{3}$). In $CoGe_{1.5}Te_{1.5}$, the Ge sites have some Te atoms and vice versa. (c) A four-membered rectangular ring ($[Sb_4]^4$-) in $CoSb_3$ and two crystallographically distinct diamond-like rings ($[Ge_2Te_2]^{4-}$) in $CoGe_{1.5}Te_{1.5}$.

Unlike binary skutterudites, ternary skutterudites suffer from low electrical conductivity but advance in high Seebeck coefficient and low overall thermal conductivity.[33,35-38] Volja et all.[39] applied first-principles calculations to study the

electronic band structure of both binary and ternary skutterudites. In comparison with the binary $CoSb_3$ skutterudite, $Co_4Ge_6Te_6$ and $Co_4Sn_6Te_6$ each have a higher Seebeck coefficient and a lower electrical conductivity, which were attributed to their multivalley band structure with heavy charge carriers. Also, a much lower lattice conductivity was observed in both $Co_4Ge_6Te_6$ and $Co_4Sn_6Te_6$, where the distorted four-membered ring and significant anionic disorder introduced extra phonon scattering.[39] In the past decade, an extensive amount of attention has spent on the *n*-type $Co_4Ge_6Te_6$[31,33,35,39], however, the *p*-type Co4Ge6Te6 was not investigated to a similar extend. In this work, Fe substitution on the Co site is employed to convert an *n*-type Co4Ge6Te6 into a *p*-type material, and the thermoelectric properties of the *p*-type $Co_{4-x}Fe_xGe_6Te_6$ (x = 0.04 and 0.12) is reported.

4.2. Experimental

Synthesis

Polycrystalline $Fe_xCo_{4-x}Ge_6Te_6$ samples (x = 0, 0.04, 0.12 and 0.20) were prepared from stoichiometric mixtures of cobalt (99.9 wt.%), germanium (99.99 wt.%), tellurium (99.999 wt.%) and iron (99.5 wt.%). Germanium and tellurium were ground into fine powders and mixed with the cobalt and iron powders inside an Ar-filled glovebox (O_2 and H_2O amounts were below 0.1 ppm). The mixtures were cold pressed into pellets and then loaded into carbon-coated silica tubes in the Ar-filled glovebox. The tubes were closed,

transferred to a vacuum line, evacuated below 0.002 Torr, and flamed sealed. The samples were heated at 100°C/h to 400°C and annealed at this temperature for 12 hours. This was followed by heating at 100°C/h to 1150°C, where the samples were annealed for 6 hours and then quenched in ice water. The solid products were hand-ground and cold-pressed under the atmosphere. Subsequently, it was annealed in evacuated silica tubes at 610 °C for 96 hours and quenched in ice water. The last annealing process was repeated one more time to eliminate the impurity phases.

Spark Plasma Sintering (SPS)

The annealed samples were finely ground into powders and loaded into a 15 mm diameter graphite die. A layer of mica paper was placed between the sample and graphite plungers to avoid direct current in the perpendicular direction. The samples were heated at 100°C/min to 550°C and annealed for 25 minutes under the uniaxial pressure of 45 MPa, followed by cooling to room temperature.

X-ray Powder Diffraction

The powder X-ray diffraction (PXRD) analysis was carried out in a PANalytical X'Pert Pro diffractometer with the CuKα_1 radiation and an X'Celerator detector. The samples were ground into a fine powder and loaded on a zero-background silicon disc. The diffraction data were collected in the 2θ range of 20° to 80° at room temperature. The sample purity and lattice

parameters were determined by the Rietveld refinement (Rietica software[40]). The profile parameters (background, peak shape), lattice parameters, and sample displacement were refined. The atomic parameters and occupancies were taken from the work by Vaqueiro et al. (for $Co_4Ge_6Te_6$)[34], Betzembroeck et al. (for CoTe)[41], Muhler et al. (for $CoTe_2$)[42], and Samanta et al. (for GeTe)[43], and were not refined.

Thermoelectric Measurements

SPS pellets were cut into rectangular bars (3mm × 3mm × 10mm) for the Seebeck coefficient and electrical conductivity measurements or into squares (10mm × 10mm × 1mm) for thermal conductivity, Hall carrier concentration, and mobility measurements. The sample was cut on a low-speed diamond saw, and kerosene was used as a lubricant to prevent sample oxidation during cutting.

Electrical conductivity and Seebeck coefficient measurements were carried out on a ULVAC-RIKO ZEM-3 instrument. A Netzsch LFA 457 instrument was used to collect the thermal diffusivity (D) of samples, and the total thermal conductivity was calculated by $\kappa total = D \times Cp \times \rho$. The standard sample (pyroceram) was used as a reference for the temperature-dependent specific heat capacity Cp measurements. The density ρ of the $Co_{3.88}Fe_{0.12}Ge_6Te_6$ sample was measured by the Archimedes method, and it was 96.8% of the theoretical density.

Hall effect measurements

The Hall coefficients RH were measured by the Van der Pauw method in an MMR Variable Temperature Hall System (VTHS) modified with AC excitation and detection from a Stanford Research SR830 lock-in amplifier. The magnetic field (B) swapped from -1.3T to 1.3T, and the AC current (I) was fixed at 5 mA. The Hall coefficient was calculated from $R_H = \frac{t \times V_H}{I \times B}$, where t is the thickness of the sample and V_H is the Hall voltage measured at room temperature. A scatter graph plotted with the V_H as the y axis and B as the x axis was used to obtain a linear fit, the slope of which allowed the Hall coefficient to be derived. The Hall carrier mobility μ_H was calculated by$\mu_H = \frac{R_H}{\rho}$, where ρ is the sheet resistance and the hole concentration was calculated based on the equation of $n_p = \frac{1}{eR_H}$ where e is the elementary charge.

4.3. Results and Discussion

Among the binary skutterudites, the *p*-type $CoSb_3$-based materials have been extensively studied[45-48] due to their excellent electrical properties and relatively simple solid state synthesis. Among the ternary mixed anion skutterudites, the *n*-type $Co_4Ge_6Te_6$ received a lot of attention as it has a higher Seebeck coefficient[49] and a lower thermal conductivity than the binary $CoSb_3$.[50] However, the development of *p*-type $Co_4Ge_6Te_6$ was

challenging, mainly attributed by the difficulty in the synthetic procedures. This work describes our efforts to convert *n*-type $Co_4Ge_6Te_6$ into a *p*-type material via partial Fe substitution. Our approach relies on the idea that Fe will adopt a 3+ oxidation state like Co. Still because of its lower electron count (*d*5 in Fe^{3+} vs. *d*6 in Co^{3+}), the Fermi level in the Fe-substituted $Co_4Ge_6Te_6$ will shift into the valence band, leading to the *p*-type conductivity.

Based on the room temperature X-ray powder diffraction patterns (Figure 4.2), $Co_{4-x}Fe_xGe_6Te_6$ (x = 0, 0.04, 0.12 and 0.20) adopts a rhombohedral symmetry ($R\bar{3}$). Three impurity phases, CoTe (*Pnnm*), CoTe2(*P*63*/mmc*), and GeTe (*R*3*m*), could be detected in a small trace. The sample purity and lattice parameter were determined by the Rietveld refinement (Rietica software)[40], and the refinement results are shown in Table 4.1. With an increasing Fe amount, the cell volume of $Co_{4-x}Ge_6Te_6$ (x = 0, 0.04, and 0.12) goes up, which can be attributed to a slightly larger effective cationic radius of Fe^{3+} (0.55Å vs. 0.545Å for Co^{3+}).[51] The smaller cell volume for x = 0.2 in comparison to x = 0.12 suggests that the solubility limit for $Co_{4-x}Fe_xGe_6Te_6$ has already been reached, and some non-equilibrium processes occur in the sample. While the Fe impurities could be suspected in the $Co_{3.80}Fe_{0.20}Ge_6Te_6$ sample, the concentration of elemental Fe could not be reliably

refined due to the overlap of the most intensive (110) peak of Fe with the peaks from $Co_{4-x}Fe_xGe_6Te_6$ and CoTe.

Table 4.1. *R* profile values, unit cell volume and impurity phases of $Co_{4-x}Fe_xGe_6Te_6$ (x = 0, 0.04, 0.12 and 0.2)

Composition	*Rp, %*	Cell volume, Å3	Impurity phases (molar %)
$Co_4Ge_6Te_6$	4.63	1988.15(7)	CoTe~ 0.02 (1) $CoTe_2$~ 0.07 (2) GeTe~0.2(1)
$Co_{3.96}Fe_{0.04}Ge_6Te_6$	4.80	1988.55(9)	CoTe~ 0.03 (2) $CoTe_2$~ 0.2 (1) GeTe~0.2(1)
$Co_{3.88}Fe_{0.12}Ge_6Te_6$	7.06	1989.49(9)	CoTe~ 0.15 (2) $CoTe_2$~ 0.3(1) GeTe~0.3(1)
$Co_{3.80}Fe_{0.20}Ge_6Te_6$	6.46	1989.08(6)	CoTe~ 0.28 (3) $CoTe_2$~ 0.9 (1)

Electrical conductivity, Seebeck coefficient, and power factor of the Fe-substituted samples in comparison to pristine Co4Ge6Te6 are shown in Fig.4.2 (b-d). Fe substitution leads to an increase in electrical conductivity. The electrical conductivity of $Co_{3.8}Fe_{0.2}Ge_6Te_6$ almost equals that of $Co_{3.88}Fe_{0.12}Ge_6Te_6$, once again suggesting a solubility limit has been reached before x=0.20. For all Fe-doped samples, the electrical conductivity decreases with an increasing temperature from 150 to 400 or 450°C, which is likely due to the phonon-electron scattering[52,53]. Above 400 or 450°C, a simultaneous increase in electrical conductivity and a decrease in the Seebeck coefficient suggest a bipolar effect.[54] The negative Seebeck coefficient of the pristine $Co_4Ge_6Te_6$ (Fig. 4.2 (c)) implies that electrons are the dominant charge carriers, and the positive values of the Fe-

substituted samples indicate that holes are the dominant carriers. These data suggest that the *n*-type Co4Ge6Te6 has been successfully converted into a *p*-type material via Fe substitution. Besides, the power factor of the Fe-substituted samples is higher than that of the pristine $Co_4Ge_6Te_6$ (Fig. 4.2(d)), and this is primarily due to the enhanced electrical conductivity.

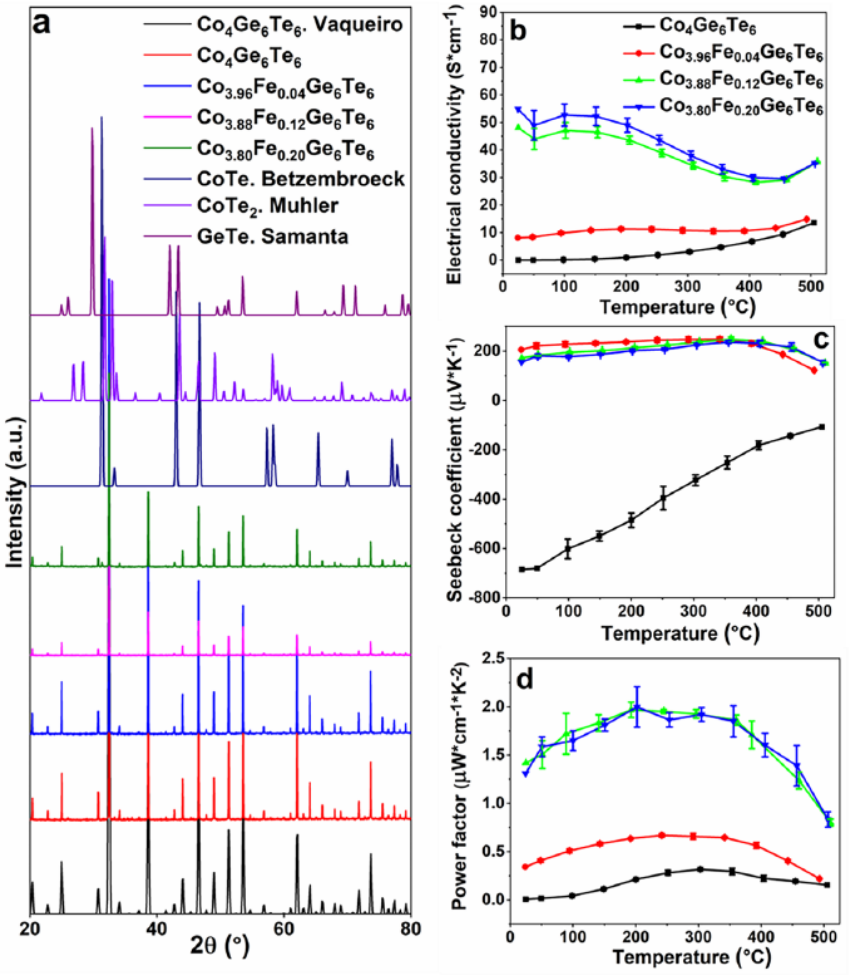

Figure 4.2. PXRD patterns of $Co_4Ge_6Te_6$[34], $Co_{4-x}Fe_xGe_6Te_6$ (x = 0, 0.04, 0.12 and 0.20), CoTe[41], CoTe2[42] and GeTe[43] at room temperature. (b) Electrical conductivity, (c) Seebeck coefficient, and (d) power factor of $Co_{4-x}Fe_xGe_6Te_6$.

We measured the Hall effect to gain further insights into the charge transport properties. The positive Hall coefficient of $Co_{4-x}Fe_xGe_6Te_6$ (x = 0.04, and 0.12, Table 4.2) indicates that holes are the dominant carriers upon the Fe substitution, thus confirming the successful conversion of the *n*-type $Co_4Ge_6Te_6$ into a *p*-type material. The carrier concentration of $Co_{4-x}Fe_xGe_6Te_6$ (x = 0, 0.04, and 0.12) increases with the additional Fe amount.

Table 4.2. Hall coefficient, Hall concentration, Hall mobility, carrier concentration, and carrier mobility of $Co_4Ge_6Te_6$, $Co_{3.96}Fe_{0.04}Ge_6Te_6$ and $Co_{3.88}Fe_{0.12}Ge_6Te_6$ at room temperature.

Composition	Hall coefficient (10^{-6} mm^3/C)	Carrier concentration (10^{18} cm^{-3})	Carrier mobility ($cm^2V^{-1}s^{-1}$)
$Co_4Ge_6Te_6$	-9.08(1)	0.68(5)	3.2(2)
$Co_{3.96}Fe_{0.04}Ge_6Te_6$	1.19(1)	5.2(1)	5.0(1)
$Co_{3.88}Fe_{0.12}Ge_6Te_6$	0.18(1)	33.0(5)	4.3(6)

$Co_{3.88}Fe_{0.12}Ge_6Te_6$ was intentionally selected for thermal properties investigation as it has the highest power factor from 50 to 500°C (Figure 4.2d) and a smaller amount of impurities than $Co_{3.80}Fe_{0.20}Ge_6Te_6$ as a solubility limit has been reached before the substitution of 5% Fe. Figure 4.3 illustrates the temperature-dependent thermal conductivities and zT values of $Co_{3.88}Fe_{0.12}Ge_6Te_6$. As shown in Figure 4.4(a), its carrier thermal conductivity, which is calculated using the Wiedemann-Franz law ($ke=L\sigma T$)[55], where L is the Lorentz factor defined from:$L = 1.5 + \exp\left(\frac{-|S|}{116}\right)$[56], can be almost neglected

from 50 to 500°C. Herein, the lattice thermal conductivity contributes majorly to the overall thermal conductivity in $Co_{3.88}Fe_{0.12}Ge_6Te_6$. The decreasing lattice thermal conductivity is attributed to the shorter phonon mean free path with increasing temperature. In the 50−500°C temperature range, the highest zT of pristine $Co_4Ge_6Te_6$ is 0.05 at 400°C[49], and the highest ZT of $Co_{3.88}Fe_{0.12}Ge_6Te_6$ is 0.12 at 400°C (Figure 4.3(b)). The low electrical conductivity is the major drawback that limits the thermoelectrical performance of $Co_{3.88}Fe_{0.12}Ge_6Te_6$

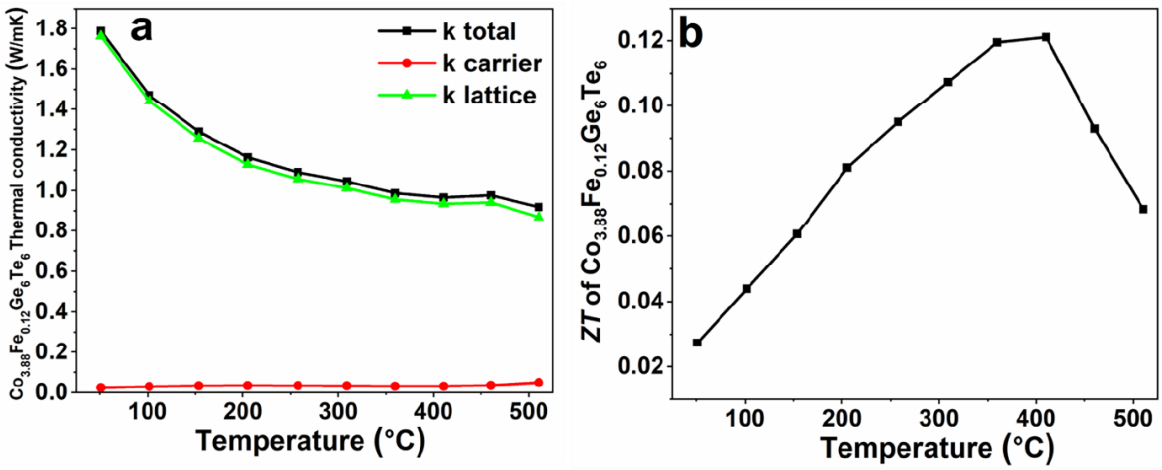

Figure 4.3 (a) Total, carrier, and lattice thermal conductivity; (b) zT values of $Co_{3.88}Fe_{0.12}Ge_6Te_6$.

4.4. Conclusion

In this study, the mixed anion skutterudites $Co_{4-x}Fe_xGe_6Te_6$ (x = 0.04 and 0.12) were synthesized, and their structural and electrical properties were investigated. The positive Seebeck and Hall coefficients observed in the Fe-substituted $Co_4Ge_6Te_6$ samples indicate

that holes are the dominant charge carriers in $Co_{4-x}Fe_xGe_6Te_6$ (x = 0.04 and 0.12). This also proves that substitution by electron-deficient atoms in Co4Ge6Te6 can convert the *n*-type $Co_4Ge_6Te_6$ into a *p*-type material. Among all the prepared samples, $Co_{3.88}Fe_{0.12}Ge_6Te_6$ performed well in thermal conductivity, and the dominant thermal conductivity is the lattice thermal conductivity from 50 to 500°C. The highest *ZT* value of 0.12 was achieved in $Co_{3.88}Fe_{0.12}Ge_6Te_6$ at 400°C. Even though a 140% improvement was reported in this study on the $Co_{3.88}Fe_{0.12}Ge_6Te_6$ over the pristine $Co_4Ge_6Te_6$, it does not meet the performance standard of thermoelectric generators for today's energy needs. The shattered electrical conductivity in the $Co_{3.88}Fe_{0.12}Ge_6Te_6$ requires further study and enhancement.

Summary and Future Directions

Among the two projects researched, the GeTe system is more mature and has been widely studied by other groups. In our work, we noticed a significant drawback in this system and applied original techniques to overcome its flaw. We successfully introduced eco-friendly ZnO into GeTe to optimize its carrier concentration and achieved a 23% average efficiency improvement. The introduced ZnO suppressed the hole concentration solely based on its chemistry, preserving the band morphology in GeTe. The product can serve as a precursor that has the potential for additional co-dopants to improve its efficiency further.

The skutterudite $Co_4Ge_6Te_6$ system has not been extensively studied and may have a large potential. In this work, novel *p*-type Fe-doped $Co_4Ge_6Te_6$ has been prepared, and the 3% iron-doped sample shows a 140% improvement over the pristine material, opening the possibility of further material optimization. As an example, the voids within the $Co_4Ge_6Te_6$ structure are still vacant, and the use of fillers can improve the thermoelectric performance of $Co_4Ge_6Te_6$.

Lastly, by reviewing the achievements in thermoelectric research, we recognized the power of computational simulations and how this technique has reshaped the field. Electronic structure analysis has guided researchers by providing them with insights into

the behavior of various dopants, thereby streamlining materials discovery and optimization. However, to fully harvest the power of computational simulations, I need to have a thorough knowledge of material physics.

References

1. T.M. Tritt, *Thermoelectric Phenomena, Materials, and Applications, Annu. Rev. Mater. Res.* 41 (2011) 433–448. https://doi.org/10.1146/annurev-matsci-062910-100453.
2. G. Tan, L.-D. Zhao, M.G. Kanatzidis, *Rationally Designing High-Performance Bulk Thermoelectric Materials, Chem. Rev.* 116 (2016) 12123–12149. https://doi.org/10.1021/acs.chemrev.6b00255.
3. G.J. Snyder, E.S. Toberer, *Complex thermoelectric materials, Nature Materials*. 7 (2008) 105–114. https://doi.org/10.1038/nmat2090.
4. J. Tang, Z. Yao, Y. Wu, S. Lin, F. Xiong, W. Li, Y. Chen, T. Zhu, Y. Pei, *Atomic disordering advances thermoelectric group IV telluride alloys with a multiband transport, Materials Today Physics.* 15 (2020) 100247. https://doi.org/10.1016/j.mtphys.2020.100247.
5. J. Tang, Z. Yao, Z. Chen, S. Lin, X. Zhang, F. Xiong, W. Li, Y. Chen, Y. Pei, *Maximization of transporting bands for high-performance SnTe alloy thermoelectrics, Materials Today Physics.* 9 (2019) 100091. https://doi.org/10.1016/j.mtphys.2019.03.005.
6. G. Tan, F. Shi, S. Hao, H. Chi, T.P. Bailey, L.-D. Zhao, C. Uher, C. Wolverton, V.P. Dravid, M.G. Kanatzidis, *Valence Band Modification and High Thermoelectric Performance in SnTe Heavily Alloyed with MnTe, J. Am. Chem. Soc.* 137 (2015) 11507–11516. https://doi.org/10.1021/jacs.5b07284.
7. L. Wang, X. Tan, G. Liu, J. Xu, H. Shao, B. Yu, H. Jiang, S. Yue, J. Jiang, Manipulating *Band Convergence and Resonant State in Thermoelectric Material SnTe by Mn–In Codoping, ACS Energy Lett. 2* (2017) 1203–1207. https://doi.org/10.1021/acsenergylett.7b00285.
8. Y. Pei, H. Wang, G.J. Snyder, *Band Engineering of Thermoelectric Materials, Adv. Mater.* 24 (2012) 6125–6135. https://doi.org/10.1002/adma.201202919.
9. A. Banik, K. Biswas, *AgI alloying in SnTe boosts the thermoelectric performance via simultaneous valence band convergence and carrier concentration optimization, Journal of Solid State Chemistry.* 242 (2016) 43–49. https://doi.org/10.1016/j.jssc.2016.02.012.
10. J. Li, Z. Chen, X. Zhang, H. Yu, Z. Wu, H. Xie, Y. Chen, Y. Pei, *Simultaneous Optimization of Carrier Concentration and Alloy Scattering for Ultrahigh Performance GeTe Thermoelectrics, Adv. Sci.* 4 (2017) 1700341. https://doi.org/10.1002/advs.201700341.
11. F. Guo, *Enhanced thermoelectric performance of SnTe alloy with Ce and Li co-doping, Materials Today Physics.* (2019) 6.
12. Z. Yao, W. Li, J. Tang, Z. Chen, S. Lin, K. Biswas, A. Burkov, Y. Pei, *Solute manipulation enabled band and defect engineering for thermoelectric enhancements of SnTe, InfoMat.* 1 (2019) 571–581. https://doi.org/10.1002/inf2.12044.
13. F. Guo, B. Cui, H. Geng, Y. Zhang, H. Wu, Q. Zhang, B. Yu, S.J. Pennycook, W. Cai, J. Sui, *Simultaneous Boost of Power Factor and Figure-of-Merit in In–Cu Codoped SnTe*, (2019) 10.
14. S. Song, C.-W.T. Lo, M. Aminzare, Y.-C. Tseng, S.M. Valiyaveettil, Y. Mozharivskyj, *Enhancing the thermoelectric performance of Sn 0.5 Ge 0.5 Te via doping with Sb/Bi and alloying with Cu 2 Te: Optimization of transport properties and thermal*

conductivities, Dalton Trans. 49 (2020) 6135–6144. https://doi.org/10.1039/D0DT00544D.
15. J. Tang, B. Gao, S. Lin, J. Li, Z. Chen, F. Xiong, W. Li, Y. Chen, Y. Pei, *Manipulation of Band Structure and Interstitial Defects for Improving Thermoelectric SnTe, Adv. Funct. Mater.* 28 (2018) 1803586. https://doi.org/10.1002/adfm.201803586.
16. X. Zhang, Y. Zhou, Y. Pei, Y. Chen, B. Yuan, S. Zhang, Y. Deng, S. Gong, J. He, L.-D. Zhao, *Enhancing thermoelectric performance of SnTe via nanostructuring particle size, Journal of Alloys and Compounds*. 709 (2017) 575–580. https://doi.org/10.1016/j.jallcom.2017.02.283.
17. Z. Luo, X. Zhang, X. Hua, G. Tan, T.P. Bailey, J. Xu, C. Uher, C. Wolverton, V.P. Dravid, Q. Yan, M.G. Kanatzidis, *High Thermoelectric Performance in Supersaturated Solid Solutions and Nanostructured n-Type PbTe–GeTe, Adv. Funct. Mater.* 28 (2018) 1801617. https://doi.org/10.1002/adfm.201801617.
18. M. Samanta, S. Roychowdhury, J. Ghatak, S. Perumal, K. Biswas, *Ultrahigh Average Thermoelectric Figure of Merit, Low Lattice Thermal Conductivity and Enhanced Microhardness in Nanostructured (GeTe) x (AgSbSe 2) 100− x , Chem. Eur. J*. 23 (2017) 7438–7443. https://doi.org/10.1002/chem.201701480.
19. J.-P. Fleurial, T. Caillat, A. Borshchevsky, *Skutterudites: A new class of promising thermoelectric materials*, in: *AIP Conference Proceedings*, AIP, Kansas City, Missouri (USA), 1994: pp. 40–44. https://doi.org/10.1063/1.46831.
20. J.-P. Fleurial, T. Caillat, A. Borshchevsky, *Skutterudites: an update, in: XVI ICT '97. Proceedings ICT'97. 16th International Conference on Thermoelectrics* (Cat. No.97TH8291), IEEE, Dresden, Germany, 1997: pp. 1–11. https://doi.org/10.1109/ICT.1997.666968.
21. C. Artini, R. Carlini, R. Spotorno, F. Failamani, T. Mori, P. Mele, *Structural Properties and Thermoelectric Performance of the Double-Filled Skutterudite (Sm,Gd)y(FexNi1-x)4Sb12, Materials.* 12 (2019) 2451. https://doi.org/10.3390/ma12152451.
22. Z.-Y. Liu, J.-L. Zhu, X. Tong, S. Niu, W.-Y. Zhao, *A review of CoSb3-based skutterudite thermoelectric materials, J Adv Ceram.* 9 (2020) 647–673. https://doi.org/10.1007/s40145-020-0407-4.
23. M. Hamid Elsheikh, D.A. Shnawah, M.F.M. Sabri, S.B.M. Said, M. Haji Hassan, M.B. Ali Bashir, M. Mohamad, *A review on thermoelectric renewable energy: Principle parameters that affect their performance, Renewable and Sustainable Energy Reviews.* 30 (2014) 337–355. https://doi.org/10.1016/j.rser.2013.10.027.
24. V.L. Kuznetsov, L.A. Kuznetsova, D.M. Rowe, *Effect of partial void filling on the transport properties of Nd x Co 4 Sb 12 skutterudites, J. Phys.: Condens. Matter*. 15 (2003) 5035–5048. https://doi.org/10.1088/0953-8984/15/29/315.
25. L.D. Chen, T. Kawahara, X.F. Tang, T. Goto, T. Hirai, J.S. Dyck, W. Chen, C. Uher, *Anomalous barium filling fraction and n -type thermoelectric performance of BayCo4Sb12, Journal of Applied Physics*. 90 (2001) 1864–1868. https://doi.org/10.1063/1.1388162.

26. G.S. Nolas, M. Kaeser, R.T. Littleton, T.M. Tritt, *High figure of merit in partially filled ytterbium skutterudite materials, Appl. Phys. Lett.* 77 (2000) 1855. https://doi.org/10.1063/1.1311597.
27. X. Shi, J. Yang, J.R. Salvador, M. Chi, J.Y. Cho, H. Wang, S. Bai, J. Yang, W. Zhang, L. Chen, *Multiple-Filled Skutterudites: High Thermoelectric Figure of Merit through Separately Optimizing Electrical and Thermal Transports, J. Am. Chem. Soc.* 133 (2011) 7837–7846. https://doi.org/10.1021/ja111199y.
28. M. Matsubara, R. Asahi, *Optimization of Filler Elements in CoSb3-Based Skutterudites for High-Performance n-Type Thermoelectric Materials, Journal of Elec Materi*. 45 (2016) 1669–1678. https://doi.org/10.1007/s11664-015-4155-0.
29. H. Luo, *A large family of filled skutterudites stabilized by electron count, NATURE COMMUNICATIONS.* (2015) 10.
30. R. Korenstein, S. Soled, A. Wold, G. Collin, *Preparation and characterization of the skutterudite-related phases CoGe1.5S1.5 and CoGe1.5Se1.5, Inorg. Chem.* 16 (1977) 2344–2346. https://doi.org/10.1021/ic50175a038.
31. P. Vaqueiro, G.G. Sobany, A.V. Powell, K.S. Knight, *Structure and thermoelectric properties of the ordered skutterudite CoGe1.5Te1.5, Journal of Solid State Chemistry.* 179 (2006) 2047–2053. https://doi.org/10.1016/j.jssc.2006.04.004.
32. Th. Schmidt, G. Kliche, H.D. Lutz, *Structure refinement of skutterudite-type cobalt triantimonide, CoSb3, Acta Crystallogr C Cryst Struct Commun.* 43 (1987) 1678–1679. https://doi.org/10.1107/S0108270187090590.
33. A. Kaltzoglou, A.V. Powell, K.S. Knight, P. Vaqueiro, *High-temperature order–disorder transitions in the skutterudites CoGe1.5Q1.5 (Q=S, Te), Journal of Solid State Chemistry.* 198 (2013) 525–531. https://doi.org/10.1016/j.jssc.2012.11.025.
34. P. Vaqueiro, G.G. Sobany, A.V. Powell, *A synchrotronpowder X-ray diffraction study of the skutterudite-related phases AB 1.5 Te 1.5 (A = Co, Rh, Ir; B = Ge, Sn), Dalton Trans.* 39 (2010) 1020–1026. https://doi.org/10.1039/B913578B.
35. M. Aminzare, Y.-C. Tseng, Y. Mozharivskyj, *Effect of spark plasma sintering and Sb doping on the thermoelectric properties of Co4Ge6Te6 skutterudite, Journal of Solid State Chemistry*. 269 (2019) 434–441. https://doi.org/10.1016/j.jssc.2018.10.020.
36. Y. Liang, B. Fang, X.M. Zhu, M.M. Liang, *Superstructure and physical properties of skutterudite-related phase CoGe 1.5 Se 1.5, IOP Conf. Ser.: Mater. Sci. Eng.* 182 (2017) 012012. https://doi.org/10.1088/1757-899X/182/1/012012.
37. Y. Dong, K. Wei, G.S. Nolas, *Transport properties of partially filled skutterudite derivatives Ce 0.13 Co 4 Ge 6 Se 6and Yb 0.14 Co 4 Ge 6 Se 6, Phys. Rev. B*. 87 (2013) 195203. https://doi.org/10.1103/PhysRevB.87.195203.
38. A. Zevalkink, K. Star, U. Aydemir, G.J. Snyder, J.-P. Fleurial, S. Bux, T. Vo, P. von Allmen, *Electronic structure and thermoelectric properties of pnictogen-substituted A Sn 1.5 Te 1.5 (A = Co, Rh, Ir) skutterudites, Journal of Applied Physics.* 118 (2015) 035107. https://doi.org/10.1063/1.4926479.
39. D. Volja, B. Kozinsky, A. Li, D. Wee, N. Marzari, M. Fornari, *Electronic, vibrational, and transport properties of pnictogen-substituted ternary skutterudites, Phys. Rev. B*. 85 (2012) 245211. https://doi.org/10.1103/PhysRevB.85.245211.
40. B.A. Hunter, *A Visual Rietveld Program*, in: 1998.

41. P. de Meester de Betzembroeck, J. Naud, *Étude par Diffraction-X de Quelques Composés du Système Nicote Obtenus par Synthèse Thermique, Bull. Soc. Chim. Belges.* 80 (2010) 107–116. https://doi.org/10.1002/bscb.19710800112.
42. M. Muhler, W. Bensch, M. Schur, *Preparation, crystal structures, experimental and theoretical electronic band structures of cobalt tellurides in the composition range, J. Phys.*: *Condens. Matter.* 10 (1998) 2947–2962. https://doi.org/10.1088/0953-8984/10/13/012.
43. M. Samanta, T. Ghosh, R. Arora, U.V. Waghmare, K. Biswas, *Realization of Both n- and p-Type GeTe Thermoelectrics: Electronic Structure Modulation by AgBiSe 2 Alloying, J. Am. Chem. Soc.* 141 (2019) 19505–19512. https://doi.org/10.1021/jacs.9b11405.
44. O.K. Andersen, Z. Pawlowska, O. Jepsen, *Illustration of the linear-muffin-tin-orbital tight-binding representation: Compact orbitals and charge density in Si, Phys. Rev. B*. 34 (1986) 5253–5269. https://doi.org/10.1103/PhysRevB.34.5253.
45. R. Liu, J. Yang, X. Chen, X. Shi, L. Chen, C. Uher, *p-Type skutterudites RxMyFe3CoSb12 (R, M = Ba, Ce, Nd, and Yb): Effectiveness of double-filling for the lattice thermal conductivity reduction, Intermetallics.* 19 (2011) 1747–1751. https://doi.org/10.1016/j.intermet.2011.06.010.
46. L. Zhou, P. Qiu, C. Uher, X. Shi, L. Chen, *Thermoelectric properties of p-type YbxLayFe2.7Co1.3Sb12 double-filled skutterudites, Intermetallics*. 32 (2013) 209–213. https://doi.org/10.1016/j.intermet.2012.08.005.
47. T. Dahal, S. Gahlawat, Q. Jie, K. Dahal, Y. Lan, K. White, Z. Ren, *Thermoelectric and mechanical properties on misch metal filled p-type skutterudites Mm0.9Fe4−xCoxSb12, J. Appl. Phys.* 117 (2015) 055101. https://doi.org/10.1063/1.4906954.
48. G. Rogl, A. Grytsiv, P. Rogl, E. Bauer, M. Zehetbauer, *A new generation of p-type didymium skutterudites with high ZT, Intermetallics.* 19 (2011) 546–555. https://doi.org/10.1016/j.intermet.2010.12.001.
49. *High-temperature order–disorder transitions in the skutterudites CoGe1.5Q1.5 (Q=S, Te) - ScienceDirect, (n.d.).* https://www.sciencedirect.com/science/article/pii/S0022459612007098 (accessed October 18, 2019).
50. Y. Kawaharada, K. Kurosaki, M. Uno, S. Yamanaka, *Thermoelectric properties of CoSb3, Journal of Alloys and Compounds.* 315 (2001) 193–197. https://doi.org/10.1016/S0925-8388(00)01275-5.
51. C. Giacovazzo, *Fundamentals of Crystallography, 3rd ed., IUCr/Oxford University Press*, 2011.
52. A. Sergeev, V. Mitin, *Electron-phonon interaction in disordered conductors: Static and vibrating scattering potentials, Phys. Rev. B*. 61 (2000) 6041–6047. https://doi.org/10.1103/PhysRevB.61.6041.
53. J.W. Sharp, H.J. Goldsmid, *Boundary scattering of charge carriers and phonons, in: Eighteenth International Conference on Thermoelectrics. Proceedings*, ICT'99 (Cat. No.99TH8407), IEEE, Baltimore, MD, USA, 1999: pp. 709–712. https://doi.org/10.1109/ICT.1999.843484.

54. S. Foster, N. Neophytou, *Doping Optimization for the Power Factor of Bipolar Thermoelectric Materials, Journal of Elec Materi*. 48 (2019) 1889–1895. https://doi.org/10.1007/s11664-018-06857-1.
55. M. Jonson, G.D. Mahan, *Mott's formula for the thermopower and the Wiedemann-Franz law, Phys. Rev. B. 21 (1980) 4223–4229. https://doi.org/10.1103/PhysRevB*.21.4223.
56. H.-S. Kim, Z.M. Gibbs, Y. Tang, H. Wang, G.J. Snyder, *Characterization of Lorenz number with Seebeck coefficient measurement, APL Materials*. 3 (2015) 041506. https://doi.org/10.1063/1.4908244.